



UNIVERSITY OF NOVI SAD
FACULTY OF SCIENCES
DEPARTMENT OF MATHEMATICS AND
INFORMATICS



SUNČICA SAKIĆ

Modelling Light Propagation In Ocular Tissues

– MASTER'S THESIS –

2020, NOVI SAD

ACKNOWLEDGEMENTS/ZAHVALNICA

First of all, I would like to express my sincere gratitude to Prof. Adérito Araújo for his continuous support, encouragement and guidance throughout this research, as well as for his emotional support and concern. The current form of this thesis would never be achieved without his assistance.

I am thankful to the other members of the research project under the same name as this thesis title, who gave me useful advices and suggestions.

Thanks also to my flatmates, Jéssica and Inês, for their friendliness and willingness to help in any situation. I learned a lot from them about Portugal and Portuguese culture.

Finally, special thanks to my friend Milica for long walks and talks in hilly Coimbra, constant support and stimulation during this tough times that marked year 2020.

Muito obrigada.

Želela bih najpre da se zahvalim članovima komisije.

Naime, veliko hvala prof. dr Srboljubu Simiću, prvenstveno na ogromnoj podršci od samog početka master studija, a potom na mnogobrojnim savetima i prenetom znanju iz Mehanike kontinuuma.

Veliku zahvalnost dugujem prof. dr Marku Nedeljkovu. Njegov uticaj je značajno doprineo razvoju moje karijere. Uz njegovu pomoć sam dobila priliku da učestvujem u međunarodnom projektu i putujem kao student. Profesorova predavanja će mi zauvek ostati u sećanju.

Posebna zahvalnost dr Ivani Vojnović kako na prenesenom znanju iz raznih predmeta tokom celokupnih studija, tako i na savetima, sugestijama i pomoći tokom izrade ovog rada. Hvala na konstantnoj podršci i strpljenju.

Ovom prilikom bih se, takođe, zahvalila prof. dr Nataši Krejić, prof. dr Danijeli Rajter-Ćirić i dr Milani Čolić na savetima, prenesenom znanju i svemu što su učinile za mene tokom master studija.

Potom bih se zahvalila svim svojim kolegama, naročito kolegama Vladimiru i Nikoli, što na prijateljstvu i razumevanju, te na korisnim diskusijama tokom protekle dve godine.

Hvala mnogo svim mojim prijateljima, posebno drugarici Mirki koja mi je potpora već deceniju.

Konačno, najveću zahvalnost dugujem svojoj porodici, posebno ocu i majci bez kojih ne bih postala ono što jesam.

Hvala mnogo.

Sunčica Sakić

ABSTRACT

In the past few decades, the medical imaging techniques have made significant contribution to the revealing of internal body structures as well as the diagnosis and treatment of disease. Specifically, in ophthalmology, one of the popular non-invasive means of ocular tissue imaging is the Optical Coherence Tomography (OCT).

In this thesis we deal with the modelling of the corneal tissue whose opacity is subject of interest among scientists still today. Our goal is to generate a virtual OCT scan using an appropriate mathematical model which could further locate conditions that lead to clouding of the human cornea.

Since eye's structures, in physical sense, represent anisotropic materials, the model requires the study of such materials. Although the numerical analysis, present in the literature, is restricted to isotropic materials, we will modify the computational tool to the anisotropic case.

Comprehension of optical eye's properties is certainly necessary to establish a mathematical model. For the purpose of numerical simulations and analysis of the numerical algorithm, different types of boundary conditions encountered in electromagnetism are considered.

Numerical simulations are performed by applying so-called Runge-Kutta discontinuous Galerkin method on Maxwell's equations previously adapted to the model. A detailed analysis of obtained results is presented.

A large part of thesis is occupied by the proposition of discontinuous Galerkin (DG) method, a procedure that belongs to the family of finite element methods. The DG method is applied on spatial discretization, while an explicit Runge-Kutta method is employed for temporal integration. In this way we get a full discretization of initial equations. In addition, convergence and stability of these methods are well studied and numerically tested on various schemes defined on different meshes.

IZVOD

U proteklih nekoliko decenija, tehnike medicinskog snimanja značajno su doprinele otkrivanju unutrašnjih telesnih struktura, kao i dijagnozi i lečenju bolesti. Konkretno, u oftalmologiji, jedan popularan neinvazivan vid snimanja očnih tkiva je optička koherentna tomografija (*engl.* Optical Coherence Tomography – OCT).

U ovoj tezi bavimo se modeliranjem tkiva rožnjače, čija neprozirnost i dan danas predstavlja predmet naučnog interesovanja. Naš cilj je generisati virtuelni OCT snimak, uz pomoć odgovarajućeg matematičkog modela, koji bi dalje mogao locirati uslove koji dovode do zamućenja ljudske rožnjače.

Kako očna tkiva predstavljaju, fizički gledano, anizotropne materijale, model zahteva izučavanje istih. Iako je numerička analiza, prisutna u literaturi, ograničena na izotropne materijale, uspeali smo modifikovati numerički alat anizotropnom slučaju.

Mehanička svojstva oka smo upotpunili uvođenjem optičkih karakteristika anizotropnih materijala, što je neophodno za razumevanje matematičkog modela u celosti. U svrhu numeričkih simulacija i analize numeričkog algoritma, razmatraju se različite vrste graničnih uslova koji se susreću u elektromagnetizmu.

Numeričke simulacije se izvode primenom tzv. Runge–Kuta prekidnog Galerkinovog metoda na Maksimalne jednačine prethodno prilagođenim modelu. Predstavljena je detaljna analiza dobijenih rezultata.

Veliki deo rada čini izučavanje materije prekidnog Galerkinovog metoda (*engl.* discontinuous Galerkin – DG), procedure koja pripada metodima konačnih elemenata. DG metod se primenjuje na prostornoj diskretizaciji, dok vremenskoj promenljivoj pristupamo koristeći eksplisitni Runge–Kuta metod. Na ovaj način dobijamo potpunu diskretizaciju početnih jednačina. Konvergencija i stabilnost ovih metoda su dobro ispitani i numerički testirani na različitim šemama definisanim na različitim mrežama diskretizacije.

Contents

List of Figures	v
List of Tables	vii
List of Abbreviations	ix
Nomenclature	xi
Preface	xiii
1 Human Eye	1
1.1 Eye's structure and corneal transparency	1
1.2 Optical Coherence Tomography	3
2 Foundations of Electromagnetism	7
2.1 Electromagnetic phenomena	7
2.2 Maxwell's equations	9
2.2.1 Maxwell's curl-equations as a Conservation Law	10
2.2.2 Wave equation in terms of electric field	11
2.3 Initial, boundary and interface conditions	12
2.3.1 Continuity condition at interface	13
2.3.2 Perfect electric conductor boundary condition	14
2.3.3 Perfect magnetic conductor boundary condition	14
2.3.4 Silver-Müller absorbing boundary condition	14
2.4 Wave propagation in anisotropic medium	15
2.4.1 Dielectric permittivity tensor	15
3 Mathematical Model	17
3.1 Three-dimensional model	17
3.1.1 Soft sources scattered field formulation	18
3.2 Reduction to two dimensions	18
4 Discontinuous Galerkin Finite Element Method	21
4.1 Briefly on meshes	21
4.2 Discontinuous Galerkin formulation	22
4.2.1 Local approximation	24
4.2.2 Numerical flux	26
4.2.3 Explicit Runge-Kutta method	28
4.3 Theoretical Validation	30
4.3.1 Consistency	31
4.3.2 Stability	32
4.3.3 Discrete Stability	34

5	Numerical Results	39
5.1	DG Formulation for Maxwell's equations	39
5.2	Numerical test	41
5.2.1	Stability	42
5.2.2	Convergence	42
5.3	Modelling scattered electromagnetic wave's propagation in 2D	47
6	Conclusion	55
	References	57
	Curriculum Vitae	61

List of Figures

1.1	The scheme of the eye. Source: https://www.toppr.com/ask/question/draw-a-diagram-of-vertical-section-of-human-eye-and/	1
1.2	A cross-section scheme of the human cornea [3].	2
1.3	The scheme of the stroma organization [3].	2
1.4	The basic principle of OCT instrument [30].	4
1.5	Example of A-scan, B-scan and 3D-OCT scan [11].	4
1.6	AS-OCT scan of cornea [16].	5
2.1	Propagation of the electric and magnetic fields associated with an electromagnetic wave.	12
4.1	Structured <i>versus</i> unstructured mesh.	22
4.2	Illustration of the first six Legendre polynomials.	25
4.3	The illustration of the idea of numerical flux on the common edge (red) formed by two adjacent elements T_k and T_ℓ . If we consider the local element T_k and Eq.(4.5), the term <i>int</i> refers to superscript ‘ $-$ ’, while <i>ext</i> denotes ‘ $+$ ’.	26
4.4	Stability regions of fourth-order Runge-Kutta methods: ERK4, LSERK(5, 4) and LSERK(14, 4).	35
4.5	Spectrum of operator \mathcal{L}_h for $K = 4$ and $N = 1, 2, 3, 4$	36
4.6	Spectrum of operator \mathcal{L}_h for $K = 29$ and $N = 1, 2, 3, 4$	36
4.7	Spectrum of operator \mathcal{L}_h for $K = 4$ and $N = 5, 9, 16, 25$	36
4.8	Spectrum of operator \mathcal{L}_h for $K = 29$ and $N = 5, 9, 16, 25$. See text for discussion.	36
5.1	Example of meshes used in numerical experiments for $K = 32$ and $K = 3200$	42
5.2	Spectrum of DG operator for TE-mode of Maxwell’s equations.	43
5.3	Spectrum of DG operator in stability regions of ERK methods.	44
5.4	L^2 -error for field E_x <i>versus</i> h	46
5.5	L^2 -error for field E_x <i>versus</i> Δt	46
5.6	Stromal collagen fibrils arrangement. See text for further discussion. . .	48
5.7	Meshes used in simulations for setup given in Fig. 5.6. The mesh above contains $K = 5072$ triangles and corresponds to the left arrangement in Fig. 5.6, while the mesh below matches with the right fibrils arrangement and counts $K = 4972$ elements.	50
5.8	Time evolution of scattered electric field intensity I^{sc} . Left hand side corresponds to healthy cornea, whereas right hand side states for case of corneal illness.	51
5.9	Horizontal cut of field I^{sc} from Fig. 5.8 at $y = 0$	52
5.10	Horizontal cut of field I^{sc} from Fig. 5.8 at $y = 0.1$	53

List of Tables

4.1	The Butcher tableau.	28
4.2	Coefficients for the LSERK(5, 4) [7].	29
4.3	Coefficients for the LSERK(14, 4) method [27].	29
5.1	Description of meshes used for computations of error.	41
5.2	L^2 -error and spatial order of convergence.	45
5.3	L^2 -error and temporal order of convergence.	46

List of Abbreviations

ABC	A bsorbing B oundary C ondition
AS-OCT	A nterior S egment- O ptical C oherence T omography
BC	B oundary C onditions
CFL	C ourant- F riedrichs- L ewy
CPU	C entral P rocessing U nit
DG	D iscontinuous G alerkin
DGTD	D iscontinuous G alerkin T ime- D omain
EMC	E xtracellular M atrix C omponents
ERK	E xplicit R unge- K utta
FD-OCT	F ourier D omain- O ptical C oherence T omography
FDM	F inite D ifference M ethod
FEM	F inite E lement M ethod
FVM	F inite V olume M ethod
LGL	L egendre- G auss- L obatto
LSERK	L ow- S torage E xplicit R unge- K utta
OCT	O ptical C oherence T omography
ODE	O rdinary D ifferential E quation
PDE	P artial D ifferential E quation
PEC	P erfect E lectric C onductor
PMC	P erfect M agnetic C onductor
PML	P erfectly M atched L ayer
RKDG	R unge- K utta D iscontinuous G alerkin
SM-ABC	S ilver- M üller A bsorbing B oundary C ondition
TD-OCT	T ime D omain- O ptical C oherence T omography
TE	T ransverse E lectric

TM	T ransverse M agnetic
1D	One D imension
2D	Two D imensions
3D	Three D imensions

Nomenclature

x	scalar
\boldsymbol{x}	vector
A_x	component x of vector \boldsymbol{A}
$\hat{\boldsymbol{n}}$	outward-pointing normal vector whose dimension is determined by given context
τ	tangential component of the given vector
\boldsymbol{Q}	matrix
$\boldsymbol{\mathcal{A}}$	tensor of second order in Euclidean space
A_{xy}	xy component of matrix \boldsymbol{A} /tensor $\boldsymbol{\mathcal{A}}$
$0, \mathbf{0}, \mathbf{0}$	zero, zero vector/matrix, zero tensor
$\text{diag}(x_1, \dots, x_n)$	diagonal matrix with entries x_1, \dots, x_n
\boldsymbol{I}	identity matrix
$\lambda(A)$	eigenvalue of matrix \boldsymbol{A}
$u _S$	the restriction of function u to the set S
$\Re(z)$	real part of complex number z
$\Im(z)$	imaginary part of complex number z
z^*	complex conjugate of a complex number z
$ z $	modulus of complex number z
$\ \cdot\ $	norm
$\langle \cdot, \cdot \rangle$	inner product
\oplus	direct sum
\equiv	equivalence
\simeq	approximately or equal
$\frac{d}{dx}, '$	differential operator with respect to variable x
$\frac{\partial}{\partial x}, \partial_x$	partial differential operator with respect to variable x
J	Jacobian matrix

∇X	gradient of scalar field X
$\nabla^2 \mathbf{X}$	Laplacian of vector field \mathbf{X}
$\nabla \cdot \mathbf{X}$	divergence of vector field \mathbf{X}
$\nabla \times \mathbf{X}$	circulation of vector field \mathbf{X}

$\int_V (\cdot) dV$ integral over volume V

$\oiint_S (\cdot) d\mathbf{S}$ integral over surface S

$\oint_C (\cdot) d\ell$ integral over contour C

Preface

Vision is by far the most used of the five senses and is one of the primary means that we use to gather information from our surroundings. The main purpose of the eye is converting light from the outside world into electrical nerve impulses. The problem usually arises when the light finds additional difficulties on its way through eye. These obstacles cause an augmented light scatter and therefore a loss of information from environment. In other words, the eye is affected by a disease. Unfortunately, many of eye diseases have no early symptoms and we may see no change in our vision until the disease has become quite advanced. To avoid such a scenario, the medicine continuously tends to develop a suitable diagnostic technique which will be capable to detect changes in highly complex eye's structure at the early stadium of progress. A popular tool widely used in ophthalmological abnormalities detection is OCT scanning (see also [11, 16]).

If the first layer of an eye is blurred, a message from environment will be certainly damaged. This is the main reason why corneal transparency has been studied through history by ophthalmologists. Many theories were established, while a chronological order of some important discoveries in corneal clarity is: [21], [14], [4] and [23]. Exact conditions that led to corneal opacity are not yet fully determined. Logically reasoning says: the more opaque cornea is, the more difficulties the OCT signal finds while passes through it, and consequently an amount of the focused light is reflected back. In the very beginning of the work (Chapter 1), this question is discussed and exact terminology is provided.

The ultimate goal of this thesis is formulating and solving a computational model that treats the corneal transparency problem by measuring the backscattered light in form of electromagnetic radiation during an OCT scan. The formulation of model, which is based on medical, optical and dielectric properties of considered tissues, is proposed in Chapter 3. In fact, the model consists of a set of partial differential equations (PDEs) that govern an electromagnetic field, the famous Maxwell's equations. Thus, the main concepts about electromagnetism are provided in Chapter 2, as well as the optical properties of an anisotropic material such eye's tissues. Conditions on domain boundary are also studied. Particularly, the conditions that enable a perfect conductivity and ones that create an artificial absorption are demonstrated. At this place we remark that Maxwell's equations are recognized as PDEs of hyperbolic type. Further, the model equations are approximately solved using a numerical method.

In general, the exact solution of a PDEs that arise in real applications is either too complicated to determine in closed form or is not known to exist. The first appearance of an approximate approach to solving PDEs originates in paper [9] by Courant, Friedrichs & Lewy, published in 1928. In the following couple of decades there were developed a numerous approximate techniques for specific PDEs and the most standard and well-established of them are finite difference method (FDM), finite element method (FEM) and finite volume method (FVM).

In FDM the local solution is calculated using appropriate finite difference approximations of derivatives involved in PDE, whereas in the FVM the local solution is ap-

proximate by a constant – a cell average. From the other side, the FEM gives the global solution using piecewise continuous polynomials. Nevertheless, all of these methods have their own advantages and disadvantages. FDM is the simplest method with a quite straightforward implementation on structured meshes (see Chapter 4). Unfortunately, the implementation complexity increases if geometric flexibility is needed. Additionally, FDM is less suitable for problems with discontinuities. On the other hand, the high-order accuracy can be combined with complex geometries using FEM, but it is generally more adjusted for elliptic problems. Although FVM is well-suited for hyperbolic equations and supports resolution of complex geometries, it is unable to obtain high-order accuracy in a straightforward way on general grids. An intelligent combination of all these features leads to the discontinuous Galerkin (DG) method [15].

In 1973, Reed & Hill applied a first form of DG method to the neutron transport equation in [28]. Since then it has undergone a fast development and finds numerous applications to *e.g.* the Euler equations of gas dynamics, the shallow water equations, the equations of magneto-hydrodynamics, the compressible Navier–Stokes equation, Maxwell’s equations, *etc.* For more details about DG development we refer to [8].

The DG method is a high order accuracy method. Also, DG method is a local method, which allows a high flexibility with meshes that can handle complicated geometries. Due to its locality, discontinuous solutions can be treated as well. A main ingredient of any DG scheme is the so-called numerical flux, whose primary role is to connect adjacent elements in order to construct the global approximation. The idea of the numerical flux is taken from FVMs, where the numerical flux has the same purpose, *i.e.*, to transport the information from one local element to another.

In Chapter 4, DG method for spatial discretization is illustrated on most common type of hyperbolic PDE, a conservation law. The discretization leads to a system of ordinary differential equations (ODEs) that after need to be solved with respect to time. For that purpose, we employ a Runge–Kutta method. The rest of chapter is devoted to theoretical verification of both methods, whereas in first part of Chapter 5 the numerical experiments on Maxwell’s equations are performed. In particular, the stability and convergence are investigated using different order of polynomial approximation and various meshes. The second half of the final chapter is dedicated to the simulation of a part of corneal tissue. Theoretical and experimental results are compared.

Chapter 1

Human Eye

Motivated by a real problem partly exposed in Preface, in this chapter we first present a brief description of eye's anatomy with main focus on corneal tissues. A deeper corneal transparency problem overview and the new understandings in ophthalmology are also presented in Section 1.1. In Section 1.2, OCT scan methodology is explained.

1.1 Eye's structure and corneal transparency

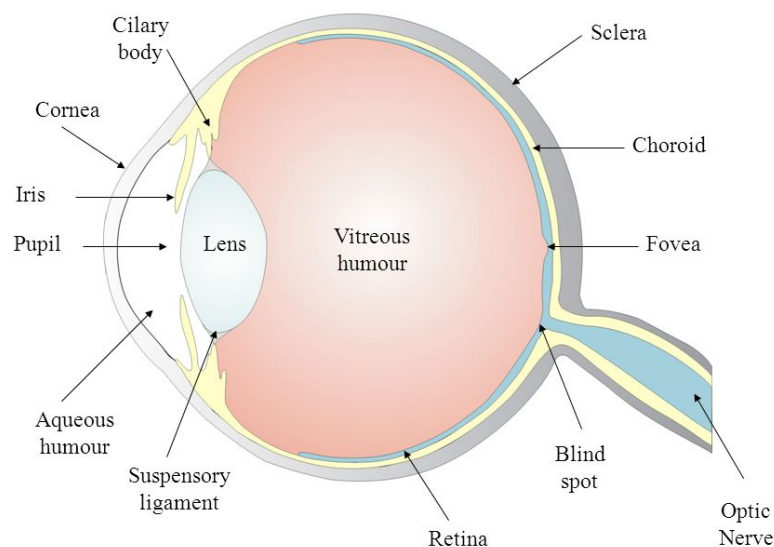


FIGURE 1.1: The scheme of the eye. Source: <https://www.toppr.com/ask/question/draw-a-diagram-of-vertical-section-of-human-eye-and/>.

The eye is a slightly asymmetrical globe composed of various tissues (see Fig. 1.1), about an inch in diameter, which possess a quite complex and sensitive mechanism. The light firstly passes *the cornea*, the clear, dome-shaped surface that covers the front of the eye and via *iris* and *pupil* goes to *lens*, which help focus light on the back of eye. Most of the eye is filled with a clear gel called *the vitreous*. The inside lining of the eye is covered by special light-sensing cells collectively called *the retina*. It converts light into electrical impulses. Behind the eye, the optic nerve carries these impulses to the brain. By virtue of a vital role in vision, the retina is subject of scientific research (see

e.g. [29]). However, in this work we are dealing with modelling corneal interaction with light, so let us describe its complexity.

The cornea is the transparent, clear layer at the front and center of the eye. Its transparency is a result of the homogeneity of the refractive index¹ of all its constituent cells. It does not contain blood vessels, unlike most of the tissues in the human body. Blood vessels may cloud the cornea, which may prevent it from refracting light properly and may adversely affect vision.

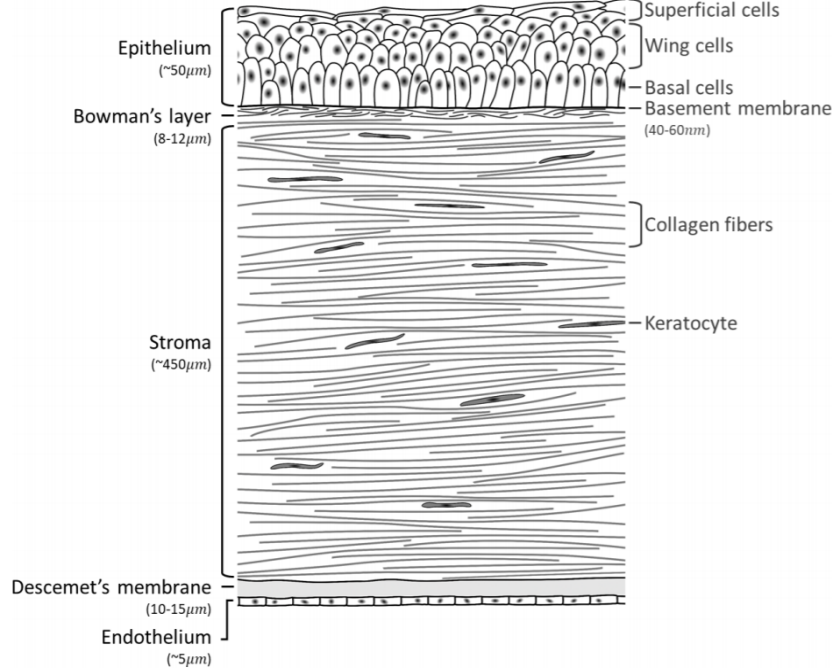


FIGURE 1.2: A cross-section scheme of the human cornea [3].

The cornea is comprised of five layers: the epithelium, Bowman's layer, the stroma, Descemet's membrane, and the endothelium (see Fig. 1.2). In normal corneas these layers are so thin that the light scattering is minimal. Many corneal pathologies are caused by changes at least in one of these layers which could lead to increased light scattering and consequent loss of corneal transparency. Clearly, the stroma is the layer that gives the eye essential strength and constitutes 90% of the cornea's thickness [3, 23].

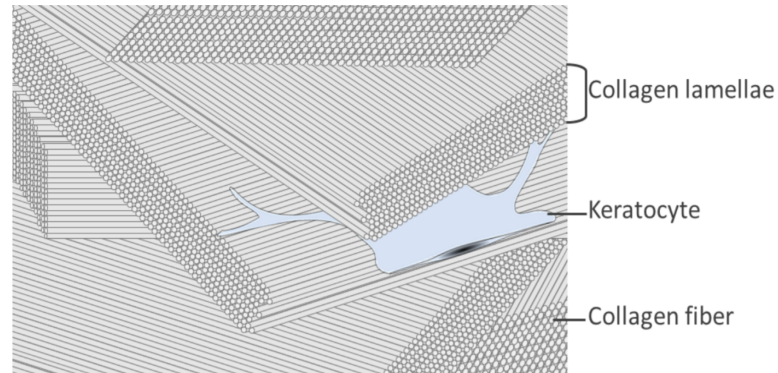


FIGURE 1.3: The scheme of the stroma organization [3].

¹In optics, the refractive index of a material is a dimensionless number that describes how fast light travels through the material. It is defined as $n = c/v$, where c is the speed of light in vacuum and v is the phase velocity of light in the medium.

The corneal stroma consists of collagens, keratocytes and other extracellular matrix components (ECM). The collagen molecules are organized into fibrils² with uniform diameters between $25nm$ and $35nm$ which are further gathered into collagen lamellae. There are from 200 to 300 lamellae of various thickness in the stroma lying parallel and interwoven together (see Fig. 1.3). Lamellae are quite interwoven in anterior region, whereas parts near Descemet's membrane seems to be less interwoven and thus the cornea there can swell easier. Getting closer to the sclera, the collagen lamellae get disorganized and therefore less transparent [23].

Since the corneal collagen fibrils cover main part of the stroma, it can be found natural that they inherit a principal role in whole cornea. Namely, collagen fibrils have to resist the tensile forces due to the intraocular pressure and protect the inner ocular tissues from external trauma while at the same time remaining narrow to allow transparency of the tissue.

The corneal transparency can be considered as a function of collagen fibrils' diameter [14]. From the other side, another key factor in corneal transparency is arrangement of collagen fibrils. Many different ideas are given on this topic [14, 21, 22, 23]. However, to ensure corneal transparency it is sufficient that the distance between adjacent fibrils be constrained.

We have to remark that the presence of the other stromal cells is ignored, *e.g.*, in [21] is given the justification that the keratocytes are sparsely distributed and are thin in the direction of the passing light.

From previous short review of corneal structure we can conclude that corneal transparency problem is reduced on transparency of corneal stroma. Since the collagen fibrils constitute the main body of stroma, we will try to construct a mathematical model that explains the corneal transparency using the uniformity of the diameters of the collagen fibrils and the range of distances between adjacent collagen fibrils.

1.2 Optical Coherence Tomography

Optical coherence tomography (OCT) is a non-invasive technique for cross-sectional tissue imaging with high and ultra-high resolution.

OCT imaging is analogous to ultrasound imaging except that it uses light instead of sound [11]. The key idea of OCT instrument lays in measuring the magnitude and echo time delay of backreflected or backscattered light from internal microstructures in tissue caused by discontinuities in its refractive index (see Fig. 1.4). Measurements of backreflection or backscattering versus depth are known as axial scans (A-scans). Cross-sectional images are generated by scanning the OCT beam in a transverse direction to acquire a series of axial scans. This generates a two-dimensional data set (B-scan) which can be displayed as a gray scale or false color image [11]. Three-dimensional volumetric data sets (3D-OCT) can be acquired by combining a series of two-dimensional data sets (B-scans). Examples of these scans are illustrated in Fig. 1.5.

OCT technology was initially introduced to the ophthalmic field for imaging of the posterior segment such as the retina and the optic nerve head. However, advancements to the technology made it possible to obtain also using OCT scan the cross-sectional images of the anterior segment of the eye (the tear film, conjunctiva, cornea, sclera, angle and lenticular structures). These techniques are collectively named by Anterior Segment Optical Coherent Tomography (AS-OCT). Images obtained by AS-OCT scan provide *in vivo*, cross-sectional views that elucidate the structural details of many conjunctival and corneal pathologies.

²In ophthalmology, some authors use expression *fiber* instead of *fibril*, as *e.g.* in [3].

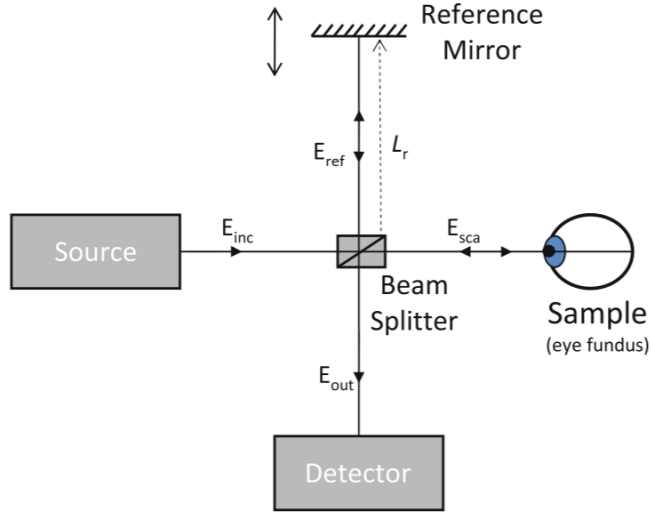


FIGURE 1.4: The basic principle of OCT instrument [30].

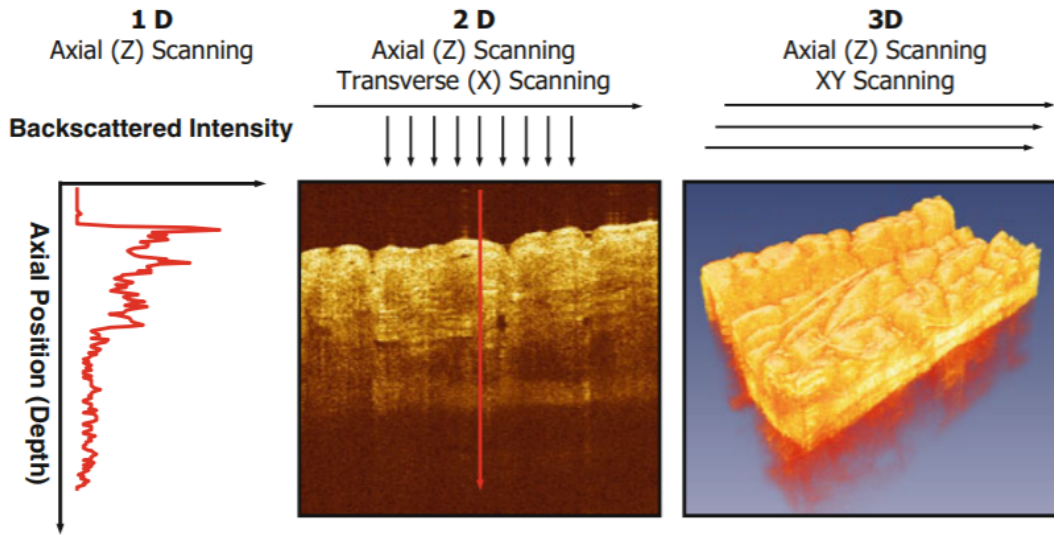


FIGURE 1.5: Example of A-scan, B-scan and 3D-OCT scan [11].

A study of corneal thickness mapping done by one of AS-OCT scan prototypes is depicted in Fig. 1.6. When the light enters in the eye, it changes its propagation direction at the interface between air and cornea due to refraction and causes significant distortion in OCT images. Image distortions due to refraction may also occur at other tissue index transition surfaces such as the cornea-aqueous interface [16]. This is indicated by red arrows in Fig. 1.6 (right).

It is worth mentioning that there are two basic types of OCT instrument: time-domain and Fourier-domain. In particular, the original OCT technology is now classified as time-domain OCT (TD-OCT), in which the reference mirror is moved through a range of delay, and the resulting interference patterns between the sample and reference beams are processed into an axial scan. From the other side, in Fourier-domain OCT (FD-OCT), the reference mirror is fixed while the interference signals from all layers of the sample are collected simultaneously using a spectral detector. Afterwards, a Fourier

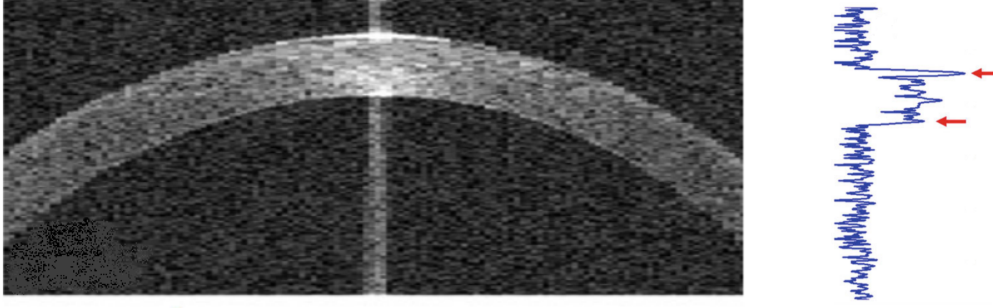


FIGURE 1.6: AS-OCT scan of cornea [16].

transform is applied to generate the A-scans [3]. Today there are many commercially available AS-OCT machines in both domains (see [16]).

Although FD-OCT usually has better performance than TD-OCT [16], we will restrict ourselves rather to time-domain and therefor develop a model based on time-domain Maxwell's equations. Thus, the electromagnetic fields need to be propagated through the optical system. Given preamble in this chapter justifies the need to study electromagnetic theory exposed in the next chapter.

Chapter 2

Foundations of Electromagnetism

In order to understand the propagation of electromagnetic waves, we need to study the equations that govern electromagnetic phenomena – Maxwell’s equations. Rather than dive straight in by writing the equations down, we begin by giving sufficient background material in this chapter.

In Section 2.1, we introduce some notion of electromagnetism. Afterwards, we present the main equations (Section 2.2) and close the system with proper conditions (Section 2.3). In Subsection 2.2.2 we find the relation with wave equation that explains a wave-like nature of main system solution, whereas in Subsection 2.2.1 we present a form of system that will be significant to us in the following chapters. Finally, in Section 2.4 we explain dielectric properties in a medium that corresponds to eye’s tissues.

2.1 Electromagnetic phenomena

Electromagnetism is the force that causes the interaction between electrically charged particles. The areas where it takes place are called electromagnetic fields. Electric fields and magnetic fields are simply different aspects of electromagnetism, and hence are intrinsically related. Moreover, a changing electric field generates a magnetic field and vice versa. This effect is called electromagnetic induction.

The classic theory mainly involves the following four time- and space-dependent vector fields:

- the electric field intensity denoted by \mathbf{E} [V/m],
- the magnetic field intensity \mathbf{H} [A/m],
- the electric displacement field (electric flux) \mathbf{D} [As/m^2],
- the magnetic induction field (magnetic flux) \mathbf{B} [Vs/m^2].

The sources of electromagnetic fields are electric charges and currents described by

- the charge density ρ [As/m^3],
- the current density function \mathbf{J} [A/m^2],

where the SI units denotes meter [m], seconds [s], Ampere [A], Volt [V] [17, 31].

Electric charge q [Am]¹ is the fundamental quantity of electricity. It can be positive or negative. It can also be zero, in which case the particle is unaffected by the force of electromagnetism. The most important property of electric charge is that it is conserved.

¹The SI unit of electric charge, Am , is also known as the coulomb [C].

In other words, the charge density can change in time only if there is a compensating current flowing into or out of that region. We express this in *the continuity equation*,

$$\frac{\partial \rho}{\partial t} + \nabla \cdot \mathbf{J} = 0. \quad (2.1)$$

In Eq.(2.1) we used the divergence operator $\nabla \cdot$ which is defined on the vector field $\mathbf{u} = \mathbf{u}(u_1, \dots, u_n)$, $u_i = u_i(x_1, \dots, x_n)$, $i = 1, \dots, n$ by

$$\nabla \cdot \mathbf{u} = \sum_{i=1}^n \frac{\partial u_i}{\partial x_i}.$$

Further, if u is a scalar field and \mathbf{u} is a vector field, we define the gradient, and the Laplacian, respectively, by

$$\begin{aligned} \nabla u &= \left(\frac{\partial u}{\partial x_1}, \dots, \frac{\partial u}{\partial x_n} \right), \\ \nabla^2 \mathbf{u} &= \sum_{i=1}^n \frac{\partial^2 u_i}{\partial x_i^2}. \end{aligned}$$

Specially, in the Euclidean space \mathbb{R}^3 we define the curl operator by

$$\nabla \times \mathbf{u} = \begin{vmatrix} \hat{\mathbf{i}} & \hat{\mathbf{j}} & \hat{\mathbf{k}} \\ \frac{\partial}{\partial x} & \frac{\partial}{\partial y} & \frac{\partial}{\partial z} \\ u_x & u_y & u_z \end{vmatrix}.$$

where $\hat{\mathbf{i}}$, $\hat{\mathbf{j}}$, and $\hat{\mathbf{k}}$ are the unit vectors for the x -, y -, and z -axes, respectively.

Before we introduce main equations we state in sequel some selected fundamental calculus theorems and vector (calculus) identities that can be found *e.g.* in [17].

THEOREM 2.1.1 (GAUSS' THEOREM) *Let $V \subset \mathbb{R}^3$ be an arbitrary volume with a piecewise smooth boundary ∂V and $\mathbf{F} \in C^1(V)$. Then*

$$\int_V (\nabla \cdot \mathbf{F}) dV = \oint_{\partial V} \mathbf{F} \cdot d\mathbf{S}. \quad (2.2)$$

THEOREM 2.1.2 (STOKES' THEOREM) *Let Γ be an arbitrary piecewise smooth closed curve and S a surface bounded by Γ . If $\mathbf{F} \in C^1(S)$, then*

$$\oint_{\Gamma} \mathbf{F} \cdot d\boldsymbol{\ell} = \iint_S (\nabla \times \mathbf{F}) \cdot d\mathbf{S}. \quad (2.3)$$

For sufficiently smooth scalar fields ψ, ϕ , and vector field \mathbf{u} is satisfied

$$\nabla \cdot (\nabla \times \mathbf{u}) = 0, \quad (2.4)$$

$$(\nabla \mathbf{u})\psi = \nabla(\mathbf{u}\psi) - \mathbf{u} \cdot \nabla \psi, \quad (2.5)$$

$$\nabla \times \nabla \times \mathbf{u} = \nabla(\nabla \cdot \mathbf{u}) - \nabla^2 \mathbf{u}, \quad (2.6)$$

$$\nabla(\psi\phi) = \psi \nabla \phi + \phi \nabla \psi, \quad (2.7)$$

$$\nabla \cdot (\psi \mathbf{u}) = \psi \nabla \cdot \mathbf{u} + (\nabla \psi) \cdot \mathbf{u}. \quad (2.8)$$

2.2 Maxwell's equations

In 1873, James Clerk Maxwell founded the modern theory of electromagnetism with publication of his ‘Treatise on Electricity and Magnetism’ [25], in which he formulated four equations intending to describe the behavior of electric and magnetic field. These equations consist of two pairs of coupled partial differential equations known as *Maxwell's equations*.

Let S be an arbitrary open surface and V an arbitrary volume. The Maxwell's equations in the integral form are given as [17]

$$\oiint_{\partial V} \mathbf{D} \cdot d\mathbf{S} = \int_V \rho dV, \quad (2.9a)$$

$$\oiint_{\partial V} \mathbf{B} \cdot d\mathbf{S} = 0, \quad (2.9b)$$

$$\oint_{\partial S} \mathbf{E} \cdot d\boldsymbol{\ell} = - \oiint_S \frac{\partial \mathbf{B}}{\partial t} \cdot d\mathbf{S}, \quad (2.9c)$$

$$\oint_{\partial S} \mathbf{H} \cdot d\boldsymbol{\ell} = \oiint_S \left(\frac{\partial \mathbf{D}}{\partial t} + \mathbf{J} \right) \cdot d\mathbf{S}. \quad (2.9d)$$

Eqs.(2.9a) and (2.9b) are *Gauss' law* for electric and magnetic field, respectively. The first equation gives the effect of the charge density on the electric displacement, whereas the second one expresses the fact that magnetic charges do not exist. The Eq.(2.9d) is *Ampere's law*, modified by Maxwell, which relates the integrated magnetic field around a closed loop to the electric current passing through the loop. The Eq.(2.9c) is known as *Faraday's law* and describes the effect of a changing magnetic field on the electric field.

Note that the integral form of the Maxwell's equations is valid almost everywhere due to nature of integral operator. In order to derive a differential form of Maxwell's equations we consider a continuous media in Eqs.(2.9). This allow us to apply Stokes' theorem, Eq.(2.3), and Gauss' theorem, Eq.(2.2). We arrive to

$$\nabla \cdot \mathbf{D} = \rho, \quad (2.10a)$$

$$\nabla \cdot \mathbf{B} = 0, \quad (2.10b)$$

$$\nabla \times \mathbf{E} = - \frac{\partial \mathbf{B}}{\partial t}, \quad (2.10c)$$

$$\nabla \times \mathbf{H} = \frac{\partial \mathbf{D}}{\partial t} + \mathbf{J}. \quad (2.10d)$$

Taking the divergence of Eq.(2.10d) in combination with Eq.(2.10a) and identity Eq.(2.4) yields us to the continuity equation (2.1). Note that the Eqs.(2.10) are not independent for time-varying fields [17].

It turns out that these equations are not sufficient to uniquely determine the electromagnetic field and additional equations are needed to model the way fields interact with the matter. First, we assume *the constitutive relations*

$$\mathbf{D} = \varepsilon \mathbf{E}, \quad \mathbf{B} = \mu \mathbf{H}, \quad \mathbf{J} = \sigma \mathbf{E},$$

where ε , μ and σ are material's permittivity, permeability and conductivity², respectively. These three parameters fully characterize the electromagnetic properties of a medium. Considering different aspects as a criterion we give the following classifications of the media [17].

- **Classification Based on the Field Dependence.** If any value of ε , μ or σ depends on the field intensities $|\mathbf{E}|^2$ and $|\mathbf{H}|^2$, the medium is called *non-linear*. Otherwise, it is called *linear*.
- **Classification Based on the Spatial Dependence.** If any of ε , μ or σ is a space-dependent function, the medium is called *inhomogeneous* or *heterogeneous*. Otherwise, it is called a *homogeneous* medium.
- **Classification Based on the Time Dependence.** If any of ε , μ or σ is a time-dependent function, the medium is called *non-stationary*. Otherwise, it is called *stationary*.
- **Classification Based on the Directions of \mathbf{D} and \mathbf{B} .** If the directions of \mathbf{D} and \mathbf{E} are parallel to each other as well as the directions of \mathbf{B} and \mathbf{H} , the medium is called *isotropic*. Otherwise, it is called an *anisotropic* medium.

We will henceforth consider $\sigma = 0$ and $\rho = 0$, which is an usual assumption in many optical researches. Taking this into account as well as the constitute relations, Eqs.(2.10c) and (2.10d) in a stationary medium become

$$\nabla \times \mathbf{E} = -\mu \frac{\partial \mathbf{H}}{\partial t}, \quad (2.11a)$$

$$\nabla \times \mathbf{H} = \varepsilon \frac{\partial \mathbf{E}}{\partial t}. \quad (2.11b)$$

The system of Eqs.(2.11) represents *the Maxwell's curl-equations*. These equations will be the equations of interest in the remaining of this thesis.

2.2.1 Maxwell's curl-equations as a Conservation Law

At the beginning of this subsection we give the most common definition of conservation law [12], so let us begin with the following system of PDEs

$$\mathbf{Q} \frac{\partial \mathbf{u}}{\partial t} + \sum_{j=1}^m \frac{\partial \mathbf{F}_j(\mathbf{u})}{\partial x_j} = \mathbf{0}, \quad (2.12)$$

where $\mathbf{u} = (u_1, \dots, u_n)^T$ with $\mathbf{u} : \Omega \times \mathbb{R}_0^+ \longrightarrow \Sigma$, where $\Omega \subset \mathbb{R}^m$ is domain of function \mathbf{u} while $\Sigma \subset \mathbb{R}^n$ is the codomain, $u_i = u_i(x_1, \dots, x_m, t)$, and $\mathbf{Q} \in \mathbb{R}^{n \times n}$. The vector \mathbf{u} is called *the state vector*, and Σ is called *the set of states*; $\mathbf{F}_j : \Sigma \longrightarrow \mathbb{R}^n$, $j = 1, \dots, m$, is called *the flux function*, where is $\mathbf{F}_j = (F_{1j}, \dots, F_{nj})^T$, and F_{ij} are smooth. We define *the flux vector* $\mathbf{F} := (F_1, \dots, F_m)$, which is a $n \times m$ -matrix, i.e.,

$$\begin{pmatrix} F_{11} & \dots & F_{1m} \\ \vdots & \ddots & \vdots \\ F_{n1} & \dots & F_{nm} \end{pmatrix}. \quad (2.13)$$

²In general, these characteristics are tensors or, mathematically speaking, 3×3 -matrices. In the rest of manuscript when needed, it will be emphasized by underlined symbol \sim that the certain parameter represents a tensor.

DEFINITION 2.2.1 The divergence $\nabla \cdot \mathbf{F} : \mathbb{R}^n \longrightarrow \mathbb{R}^n$ of a matrix field \mathbf{F} in Eq.(2.13) is defined as

$$\nabla \cdot \mathbf{F} = \left(\sum_{j=1}^m \frac{F_{ij}}{\partial x_j} \right)_{i=1}^n$$

Now we can rewrite Eq.(2.12) as

$$\mathbf{Q} \partial_t \mathbf{u} + \nabla \cdot \mathbf{F}(\mathbf{u}) = \mathbf{0}. \quad (2.14)$$

The system (2.14) is said to be in *conservative form* and it is called a *conservation law*.

DEFINITION 2.2.2 The Jacobian matrix $\mathbf{A}_j(\mathbf{u}) \in \mathbb{R}^{n \times n}$ of the flux vector components \mathbf{F}_j is defined as

$$\mathbf{A}_j(\mathbf{u}) = \left(\frac{\partial F_{ij}(\mathbf{u})}{\partial u_k} \right)_{1 \leq i, k \leq n}, \quad j = 1, \dots, m.$$

DEFINITION 2.2.3 The system of Eqs.(2.14) is hyperbolic if for all $\alpha_1, \dots, \alpha_m \in \mathbb{R}$ the matrix $\mathbf{A} := \alpha_1 \mathbf{A}_1 + \dots + \alpha_m \mathbf{A}_m$ has only real eigenvalues and is diagonalizable.

Let us come back on the Maxwell's curl-equations

$$\begin{aligned} \nabla \times \mathbf{E} &= -\underset{\sim}{\mu} \frac{\partial \mathbf{H}}{\partial t} \\ \nabla \times \mathbf{H} &= \underset{\sim}{\epsilon} \frac{\partial \mathbf{E}}{\partial t}. \end{aligned}$$

Inspired by previous definitions we define the state vector $\mathbf{u} = (\mathbf{E}, \mathbf{H})^T \in \mathbb{R}^6$ and the flux vector $\mathbf{F}(\mathbf{u}) = (\mathbf{F}_x, \mathbf{F}_y, \mathbf{F}_z)^T \in \mathbb{R}^{6 \times 3}$, where $\mathbf{F}_i = (-\hat{\mathbf{e}} \times \mathbf{E}, \hat{\mathbf{e}} \times \mathbf{H})^T \in \mathbb{R}^6$ for $i = x, y, z$, as well as the material matrix

$$\mathbf{Q} = \begin{pmatrix} \underset{\sim}{\epsilon} & \mathbf{0} \\ \mathbf{0} & \underset{\sim}{\mu} \end{pmatrix}.$$

Here we denoted by $\underset{\sim}{\epsilon}$, $\underset{\sim}{\mu}$ and $\mathbf{0}$ the tensor of permittivity, tensor of permeability (see Subsection 2.4.1) and zero tensor, respectively. We assume that \mathbf{Q} is invertable constant matrix, but generally, it can vary in space. Finally, we can represent Eqs.(2.11) in a conservation form as

$$\mathbf{Q} \partial_t \mathbf{u} + \nabla \cdot \mathbf{F}(\mathbf{u}) = \mathbf{0}. \quad (2.15)$$

Moreover, it can be straightforward shown that this is a hyperbolic system with the eigenvalues $\lambda_1 = 0$ and $\lambda_{2,3} = \pm \frac{1}{\sqrt{\epsilon \mu}}$ (see Subsection 2.2.2) where each eigenvalue has algebraic multiplicity 2.

In the end, we have to emphasize that the possibility to reformulate the Maxwell's curl-equations in conservation form is essential to us in this work. Namely, almost entire further theoretical consideration shall be strongly leaned on it.

2.2.2 Wave equation in terms of electric field

In this subsection we derive a wave equation only for the electric field. Using similar arguments, a same thing can be obtained in magnetic terms.

For the sake of brevity, we assume that the electromagnetic field is excited by a linear stationary homogeneous medium. Let us begin by taking the curl on both sides of Eq.(2.11a) and exploiting homogeneity of the medium

$$-\underset{\sim}{\mu} \cdot \nabla \times \frac{\partial \mathbf{H}}{\partial t} = \nabla \times \nabla \times \mathbf{E}. \quad (2.16)$$

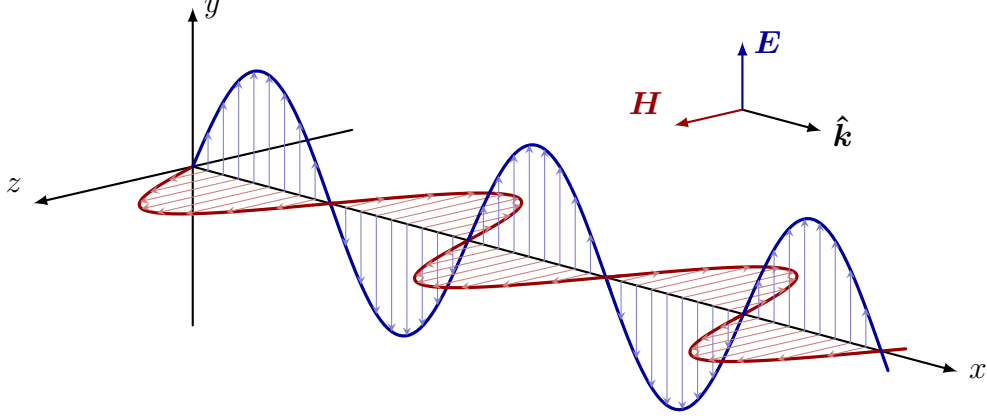


FIGURE 2.1: Propagation of the electric and magnetic fields associated with an electromagnetic wave.

An independence of differential operators ∂_t and $\nabla \times$ (*i.e.*, time and space) give us permission to interchange the order of differentiation in Eq.(2.16). Further, using Eq.(2.11a) and the stationarity of the medium we obtain

$$-\varepsilon\mu \cdot \frac{\partial^2 \mathbf{E}}{\partial t^2} = \nabla \times \nabla \times \mathbf{E}.$$

Finally, exploiting the identity Eq.(2.6) and Eq.(2.10a) we get

$$\nabla^2 \mathbf{E} - \frac{1}{c^2} \frac{\partial^2 \mathbf{E}}{\partial t^2} = \mathbf{0}. \quad (2.17)$$

Eq.(2.17) is *the wave equation* in three spatial dimensions where the quantity

$$c = \sqrt{\frac{1}{\varepsilon\mu}}$$

is *a speed of the light* or *a speed of the wave propagation*. The solutions of Eq.(2.17) are plane waves³. Note that each component of the electric field independently satisfies the wave equation.

The identification of light with an electromagnetic wave (with the velocity related to the electric permittivity and magnetic permeability) was one of the greatest achievements of 19th century physics. In 1887 Heinrich Hertz showed experimentally that electromagnetic waves consist of oscillating electric and magnetic fields in a constant phase relation perpendicular to each other and perpendicular to the direction of propagation (see Fig. 2.1), as well as that they exhibit: interference, scattering, diffraction, polarization, refraction, *etc.* Some of these waves properties will be discussed in the rest of work. First of all, let us close the system of Eqs.(2.10) with initial, boundary and interface conditions.

2.3 Initial, boundary and interface conditions

Although the number of equations now coincides with the number of unknowns, the system of differential Eqs.(2.10) is not yet complete. We have to impose initial and boundary conditions as well as interface conditions between different materials where the material parameters jump.

³This can be checked, for instance, using method of separation of variables.

In computational electromagnetism the most known conditions on boundary are reflecting, absorbing and periodic boundary conditions. In the sequel we present perfect electric conductor and perfect magnetic conductor as reflective boundary conditions, and Silver–Müller absorbing boundary conditions as absorbing ones. First of all, we introduce the interface conditions which arises from integral form of Maxwell's equations, Eqs.(2.9).

2.3.1 Continuity condition at interface

Assume a partition of the domain $V \subset \mathbb{R}^3$ into two disjoint domains V_1, V_2 such that $V = V_1 \cup V_2$. By $\Gamma := V_1 \cap V_2$ we denote the common interface, and by $\hat{\mathbf{n}}_\Gamma$ we refer to the unit normal vector pointing from V_2 to V_1 . In the following we derive the continuity requirements at interfaces by Gauss' theorem, Eq.(2.2), and Stokes' theorem, Eq.(2.3), assuming that the involved functions, domains and surfaces are sufficiently smooth. Followed by Eq.(2.9b) we obtain

$$\begin{aligned} 0 &= -\oint_{\partial V} \mathbf{B} \cdot \hat{\mathbf{n}} dS + \oint_{\partial V_1} \mathbf{B}_1 \cdot \hat{\mathbf{n}} dS + \oint_{\partial V_2} \mathbf{B}_2 \cdot \hat{\mathbf{n}} dS \\ &= \oint_{\partial V_1 \cap \Gamma} \mathbf{B}_1 \cdot \hat{\mathbf{n}}_\Gamma^- dS + \oint_{\partial V_2 \cap \Gamma} \mathbf{B}_2 \cdot \hat{\mathbf{n}}_\Gamma^+ dS \\ &= \oint_{\Gamma} \llbracket \mathbf{B} \cdot \hat{\mathbf{n}}_\Gamma \rrbracket dS, \end{aligned}$$

where $\mathbf{B}_1 := \mathbf{B}|_{V_1}$, $\mathbf{B}_2 := \mathbf{B}|_{V_2}$, and $\llbracket \mathbf{B} \cdot \hat{\mathbf{n}}_\Gamma \rrbracket = \mathbf{B}_1 \cdot \hat{\mathbf{n}}_\Gamma^- + \mathbf{B}_2 \cdot \hat{\mathbf{n}}_\Gamma^+$ denotes the jump over the interface Γ . Since the above formula is valid for arbitrary subsets of V , we obtain that the normal component of the induction field has to be continuous over the interface, which reads as

$$\llbracket \mathbf{B} \cdot \hat{\mathbf{n}}_\Gamma \rrbracket = 0. \quad (2.18)$$

A similar argument works for the electric flux density \mathbf{D} , so from Eq.(2.9a) and $\rho = 0$ we have

$$\llbracket \mathbf{D} \cdot \hat{\mathbf{n}}_\Gamma \rrbracket = 0. \quad (2.19)$$

Next we derive interface conditions for the electric field \mathbf{E} . Let the interface Γ be as above and S denote an arbitrary plane surface intersecting the interface Γ along a line $L := S \cap \Gamma$. Let $S_1 := S \cap V_1$, $S_2 := S \cap V_2$ be the two disjoint parts of S such that $S_1 \cup S_2 = S$ and $S_1 \cap S_2 = L$. Led by Eq.(2.11a) we derive

$$\begin{aligned} 0 &= -\oint_{\partial S} \mathbf{E} \cdot \boldsymbol{\tau} ds + \oint_{\partial S_1} \mathbf{E}_1 \cdot \boldsymbol{\tau}_1 ds + \oint_{\partial S_2} \mathbf{E}_2 \cdot \boldsymbol{\tau}_2 ds \\ &= \int_{S_1 \cap \Gamma} \mathbf{E}_1 \cdot \boldsymbol{\tau}_1 ds + \int_{S_2 \cap \Gamma} \mathbf{E}_2 \cdot \boldsymbol{\tau}_2 ds \\ &= \int_L \llbracket \mathbf{E} \cdot \boldsymbol{\tau}_L \rrbracket ds, \end{aligned}$$

with $\mathbf{E}_1 := \mathbf{E}|_{S_1}$ and $\mathbf{E}_2 := \mathbf{E}|_{S_2}$ and $\boldsymbol{\tau}_L = \boldsymbol{\tau}_1 = -\boldsymbol{\tau}_2$. Since S was arbitrary, we conclude that the tangential components of the electric field have to be continuous over the interface Γ , which is equivalent to

$$\llbracket \mathbf{E} \times \hat{\mathbf{n}}_\Gamma \rrbracket = \mathbf{0}. \quad (2.20)$$

In the same way we get

$$\llbracket \mathbf{H} \times \hat{\mathbf{n}}_\Gamma \rrbracket = \mathbf{0}. \quad (2.21)$$

The Eqs.(2.18)–(2.21) depict interface conditions. Notice when the first two are satisfied, the latter two are satisfied as well [17].

2.3.2 Perfect electric conductor boundary condition

In a perfect electric conductor (PEC), electric charges are free to move without any resistance to their motion. For the electric field this means that its tangential component have to be zero. From the other side, the magnetic flux must be constant in time which can be mathematically written as

$$\begin{aligned}\mathbf{B} \cdot \hat{\mathbf{n}} &= 0, \\ \mathbf{E} \times \hat{\mathbf{n}} &= \mathbf{0}.\end{aligned}$$

The PEC-wall is in particular suitable for modelling adjacent metallic domains [17].

2.3.3 Perfect magnetic conductor boundary condition

Perfect magnetic conductors (PMC) model materials with very high permeability, where one can assume a vanishing magnetic field [17]. In fact, PMC at its boundary can only have normal magnetic field components and tangential electric field components. This property is expressed as

$$\begin{aligned}\mathbf{D} \cdot \hat{\mathbf{n}} &= 0, \\ \mathbf{H} \times \hat{\mathbf{n}} &= \mathbf{0}.\end{aligned}$$

2.3.4 Silver–Müller absorbing boundary condition

Solving the time-dependent Maxwell's equations in an unbounded domain requires the introduction of artificial absorbing boundary conditions (ABCs) to close the computational domain. Typical approaches to achieving this in FEM methods include the use of a mathematical boundary condition and the use of fictitious absorbing material layers.

The main difference between PEC-wall and ABC-wall is that the ABC assumes that a plane wave solution is incident on boundary and estimates fields strictly outside boundary by using fields only inside the boundary. ABCs are thus in general approximations, and reflect some of waves back into computational domain. The accuracy of the approximation depends on the features of the ABC and on many other parameters.

Silver–Müller absorbing boundary conditions (SM-ABC) are the first-order ABC [31] and they have a form

$$\begin{aligned}\hat{\mathbf{n}} \times \mathbf{E} + \sqrt{\frac{\mu}{\varepsilon}} \hat{\mathbf{n}} \times (\hat{\mathbf{n}} \times \mathbf{H}) &= \mathbf{0}, \\ \hat{\mathbf{n}} \times \mathbf{H} - \sqrt{\frac{\varepsilon}{\mu}} \hat{\mathbf{n}} \times (\hat{\mathbf{n}} \times \mathbf{E}) &= \mathbf{0}.\end{aligned}$$

In this context, a term ‘first-order’ is related to ABCs whose estimated value of fields outside boundary are obtained by looking back one step in time and one grid cell in space. Higher order ABCs may look back over more steps in time and more grid cells in space.

There are also and alternative approaches to realizing ABCs, such as perfectly matched layer (PML). For more about this topic, we refer to [17, 31].

2.4 Wave propagation in anisotropic medium

Since we are interested in analyzing of light's behavior in an anisotropic medium, we need to study fundamentals of *crystal optics*. The crystals, one of typical anisotropic materials, we can interpret as a highly ordered microscopic structure usually arranged in a perfect lattice. In fact, we will try to explain basic properties of their subtype, *liquid crystals*. Liquid crystals combine properties of liquids and solid crystals; a liquid crystal may flow like a liquid, but its molecules may be oriented in a crystal-like way [32].

Optical properties of liquid crystals depend on the direction of propagation and the polarization of the light. In most simple words, the role of polarization is to describe the orientation of wave's oscillations. The typical approach to analyze polarization is to track the orientation of the electric field vector during electromagnetic wave's propagation. From the other side, the direction in which light travels through an anisotropic medium is fully depicted by the dielectric permittivity tensor $\boldsymbol{\xi}$.

2.4.1 Dielectric permittivity tensor

In an anisotropic dielectric medium the vector of electric flux density \mathbf{D} is expressed as a linear combination of columns of the dielectric permittivity tensor (matrix) whose coefficients are components of the electric field \mathbf{E} vector. The dielectric tensor is Hermitian, that is $\varepsilon_{ij} = \varepsilon_{ji}^*$, $i, j = x, y, z$. Specially, in a magnetically isotropic materials (*i.e.*, when $\mathbf{B} = \mu\mathbf{H}$ where μ is a scalar function), such as our medium of interest, all elements of $\boldsymbol{\xi}$ are real, and thus dielectric tensor is symmetric and can be described by 6 (instead of 9) elements,

$$\mathbf{D} = \boldsymbol{\xi}\mathbf{E},$$

$$\begin{pmatrix} D_x \\ D_y \\ D_z \end{pmatrix} = \begin{pmatrix} \varepsilon_{xx} & \varepsilon_{xy} & \varepsilon_{xz} \\ \varepsilon_{yx} & \varepsilon_{yy} & \varepsilon_{yz} \\ \varepsilon_{zx} & \varepsilon_{zy} & \varepsilon_{zz} \end{pmatrix} \begin{pmatrix} E_x \\ E_y \\ E_z \end{pmatrix}.$$

Since every symmetric matrix is, up to choice of an orthonormal basis, a diagonal matrix, there is an orthonormal basis and diagonal matrix, $\text{diag}(\varepsilon_x, \varepsilon_y, \varepsilon_z)$ whose nonzero entries are eigenvalues of $\boldsymbol{\xi}$. The choice of coordinate axes that results in a diagonal permittivity matrix is called *the principal axes* of the material.

If two of the diagonal entries of the permittivity matrix are the same and one is different, such medium is called *uniaxial media*, whereas if all entries are different the material is called *biaxial*. From the other side, if all diagonal entries are equal, the medium becomes *isotropic*.

When light is propagating in an anisotropic medium, it is clear that the direction of the electric field will vary in space. Specially, *eigenmodes* are directions invariant in space. In the eigenmode, the electric field has direction of eigenvector. The associated eigenvalues are $\varepsilon_i = n_i^2$, $i = x, y, z$, where the indices n_i are *the principal indices of refraction* [32].

In our particular case, the lamella arrangement within the cornea causes an optical phenomenon called birefringence. Birefringence represents the difference between two refractive indices usually arising in cylindrical anyisotropic structures. However, this property plays no significant role in corneal transparency [23].

Chapter 3

Mathematical Model

Main purpose of this chapter is to describe a setup of our mathematical simulation. Starting from Maxwell's equations in three dimensions, over different electromagnetic transverse modes, we reach to soft sources scattered field formulation in 2D.

Eye's tissues represent a linear, heterogeneous, stationary, anisotropic and non-magnetic medium. As we stated above, all these characteristics are contained in dielectric permittivity and permeability tensors. In the sequel we are focused on mathematical interpretation of these terms.

3.1 Three-dimensional model

Let us recall on Eqs.(2.11)

$$\begin{aligned}\boldsymbol{\varepsilon} \frac{\partial \mathbf{E}}{\partial t} &= \nabla \times \mathbf{H}, \quad \text{in } \Omega \times [0, T], \\ \boldsymbol{\mu} \frac{\partial \mathbf{H}}{\partial t} &= -\nabla \times \mathbf{E}, \quad \text{in } \Omega \times [0, T],\end{aligned}\tag{3.1}$$

where $\mathbf{E} = (E_x, E_y, E_z)^\top$, $\mathbf{H} = (H_x, H_y, H_z)^\top$, set $\Omega \subset \mathbb{R}^3$ is bounded, while permittivity $\boldsymbol{\varepsilon}$ and (isotropic) permeability $\boldsymbol{\mu} = \mu \mathbf{I}$ are only space-dependent functions. The initial conditions are given as

$$\begin{aligned}\mathbf{E}(x, y, z, 0) &= \mathbf{E}_0(x, y, z), \\ \mathbf{H}(x, y, z, 0) &= \mathbf{H}_0(x, y, z).\end{aligned}$$

Finally, by choice of boundary conditions we closed the system of six coupled Eqs.(3.1). Namely, we have chosen SM-ABCs ones

$$\hat{\mathbf{n}} \times \mathbf{E} + \sqrt{\frac{\mu}{\varepsilon_{\text{eff}}}} \hat{\mathbf{n}} \times (\hat{\mathbf{n}} \times \mathbf{H}) = \mathbf{0},$$

where effective permittivity ε_{eff} is given in the same way as in [18]

$$\varepsilon_{\text{eff}} = \frac{\det(\boldsymbol{\varepsilon})}{\hat{\mathbf{n}}^\top \boldsymbol{\varepsilon} \hat{\mathbf{n}}}.$$

Additionally, we assume that the dielectric permittivity and permeability tensors are symmetric positive definite matrices, as well as they are uniformly bounded on domain Ω , *i.e.*, there exist constants $m_\varepsilon, M_\varepsilon, m_\mu, M_\mu > 0$ such that, for all $\mathbf{x} \in \Omega$ and every unit vector $\mathbf{v} \in \mathbb{R}^3$ is satisfied

$$m_\varepsilon \leq \mathbf{v}^\top \boldsymbol{\varepsilon}(\mathbf{x}) \mathbf{v} \leq M_\varepsilon \quad \text{and} \quad m_\mu \leq \mu(\mathbf{x}) \leq M_\mu.$$

3.1.1 Soft sources scattered field formulation

Let us denote by $(\mathbf{E}^{inc}, \mathbf{H}^{inc})$ the *incident field*, the field produced inside a space domain by sources placed outside it. If a scattering object is introduced in the domain, the field differs from the incident field forming so-called *the total field* $(\mathbf{E}^{tot}, \mathbf{H}^{tot})$. We define *the scattered field* $(\mathbf{E}^{sc}, \mathbf{H}^{sc})$ as a difference of these two fields

$$\begin{aligned}\mathbf{E}^{sc} &= \mathbf{E}^{tot} - \mathbf{E}^{inc}, \\ \mathbf{H}^{sc} &= \mathbf{H}^{tot} - \mathbf{H}^{inc}.\end{aligned}\tag{3.2}$$

Clearly, both fields are solutions of Eqs.(3.1), *i.e.*,

$$\begin{aligned}\epsilon \frac{\partial \mathbf{E}^{tot}}{\partial t} &= \nabla \times \mathbf{H}^{tot}, & \epsilon^{inc} \frac{\partial \mathbf{E}^{inc}}{\partial t} &= \nabla \times \mathbf{H}^{inc}, \\ \mu \frac{\partial \mathbf{H}^{tot}}{\partial t} &= -\nabla \times \mathbf{E}^{tot}, & \mu^{inc} \frac{\partial \mathbf{H}^{tot}}{\partial t} &= -\nabla \times \mathbf{E}^{inc}.\end{aligned}\tag{3.3}$$

Combining Eqs.(3.2)–(3.4) we arrive to the soft sources scattered field formulation of Maxwell's curl-equations

$$\begin{aligned}\epsilon \frac{\partial \mathbf{E}^{sc}}{\partial t} &= \nabla \times \mathbf{H}^{sc} - (\epsilon - \epsilon^{inc}) \frac{\partial \mathbf{E}^{inc}}{\partial t}, \\ \mu \frac{\partial \mathbf{H}^{sc}}{\partial t} &= -\nabla \times \mathbf{E}^{sc} - (\mu - \mu^{inc}) \frac{\partial \mathbf{H}^{inc}}{\partial t}.\end{aligned}\tag{3.5}$$

These equations model a problem with presence of areas which we want to be transparent to traveling waves (hence the term soft source).

3.2 Reduction to two dimensions

In order to simplify the 3D model, Eqs.(3.1), we assume that one of electromagnetic fields is homogeneous in one of its directions, *e.g.* z -direction [31]. Taking into account non-magnetivity and anisotropy of the given medium, we obtain two disjunctive sets of equations

- **Transverse Electric – TE mode.**

$$\begin{aligned}\epsilon_{xx} \frac{\partial E_x}{\partial t} + \epsilon_{xy} \frac{\partial E_y}{\partial t} &= \frac{\partial H_z}{\partial y}, \\ \epsilon_{yx} \frac{\partial E_x}{\partial t} + \epsilon_{yy} \frac{\partial E_y}{\partial t} &= -\frac{\partial H_z}{\partial x}, \\ \mu \frac{\partial H_z}{\partial t} &= \frac{\partial E_x}{\partial y} - \frac{\partial E_y}{\partial x},\end{aligned}\tag{3.6}$$

- **Transverse Magnetic – TM mode.**

$$\begin{aligned}\mu \frac{\partial H_x}{\partial t} &= -\frac{\partial E_z}{\partial y}, \\ \mu \frac{\partial H_y}{\partial t} &= \frac{\partial E_z}{\partial x}, \\ \epsilon_{zz} \frac{\partial E_z}{\partial t} &= \frac{\partial H_y}{\partial x} - \frac{\partial H_x}{\partial y}.\end{aligned}\tag{3.7}$$

Finally, coupling TE mode with soft source scattered field formulation we get equations which govern two-dimensional wave propagation through eye's structures

$$\begin{aligned}
\varepsilon_{xx} \frac{\partial E_x^{sc}}{\partial t} + \varepsilon_{xy} \frac{\partial E_y^{sc}}{\partial t} &= \frac{\partial H_z^{sc}}{\partial y} + (\varepsilon^{inc} - \varepsilon_{xx}) \frac{\partial E_x^{inc}}{\partial t} - \varepsilon_{xy} \frac{\partial E_y^{inc}}{\partial t}, \\
\varepsilon_{yx} \frac{\partial E_x^{sc}}{\partial t} + \varepsilon_{yy} \frac{\partial E_y^{sc}}{\partial t} &= -\frac{\partial H_z^{sc}}{\partial x} - \varepsilon_{yx} \frac{\partial E_x^{inc}}{\partial t} + (\varepsilon^{inc} - \varepsilon_{yy}) \frac{\partial E_y^{inc}}{\partial t}, \\
\mu \frac{\partial H_z^{sc}}{\partial t} &= -\frac{\partial E_y^{sc}}{\partial x} + \frac{\partial E_x^{sc}}{\partial y} + (\mu^{inc} - \mu) \frac{\partial H_z^{inc}}{\partial t}.
\end{aligned} \tag{3.8}$$

In Eqs.(3.8) the scattered field is unknown, while the incident field will be specified later. In order to avoid reflections at the boundary of the domain, this set of equations we complement with Silver–Müller absorbing boundary conditions. At the initial time moment $t = 0$, we assume the scattered field is not excited.

Chapter 4

Discontinuous Galerkin Finite Element Method

As we have seen in Subsection 2.2.1, Maxwell's equations are linear hyperbolic PDEs and they exhibit a conservation form. In this chapter we present a numerical method that efficiently deals with such problems, the Discontinuous Galerkin (DG) Finite Element Method. The DG method can be used for time and/or spatial discretization. In order to apply DG to spatial discretization of Maxwell's equations, we will explain main ideas on most simplified problems. For the time integration, we use an explicit time stepping method, the explicit low-storage Runge-Kutta method. This combination, the DG method for spatial discretization with a Runge-Kutta scheme for time-integration, is also called Runge-Kutta Discontinuous Galerkin (RKDG) method, in mathematical literature, or Discontinuous Galerkin Time-Domain (DGTD) method, in physics literature.

Since the vectorial extension, roughly speaking, manifests in increasing unknowns and equations to be solved, we restrict ourselves to the scalar case. In that sense, we gain benefit in simplicity of presentation. After giving some basic ideas related to computational meshes, we present the definition and main characteristics of the method, which covers the case of two spatial dimensions. Finally, we check the consistency, stability and convergence of the corresponding numerical scheme in one space dimension.

4.1 Briefly on meshes

Here we are going to state some of the most common concepts about meshes that can be found *e.g.* in [24]. The mesh or grid can be formulated as a discrete representation of the geometrical domain of the problem. On a 2D mesh we distinguish the following objects: *element* or *cell* which states for control volume into which domain is broken up, *node* or grid point, *edge* or boundary of a face and *face* or boundary of an element.

The grid has a significant impact on rate of convergence (or even lack of convergence), solution accuracy and CPU time needed for computations. Intuitively, more cells give higher accuracy. However, the drawback usually displays in increased amount of memory storage as well as CPU time.

There are three well-known types of mesh: structured, unstructured and hybrid mesh. Each cell in 2D *structured mesh* can be addressed by the pair of indices (i, j) . For this reason it meets difficulties when geometry of a problem gets complex. In case of *the unstructured mesh*, the cells are arranged in an arbitrary fashion, so they can handle complicated geometries. However, this is reflected in memory and CPU time requirements. Lastly, *the hybrid mesh* integrates the structured meshes and the

unstructured meshes in an efficient manner. These meshes can be *non-conformal* which means in 2D that there is a partial or zero matching of nodes at the face.

In two dimensions elements are usually chosen to be triangles or/and quadrilaterals. We shall restrict ourselves on computational domains obtained by triangulation. One example of structured and unstructured meshes generated using triangulation is illustrated in Fig. 4.1.

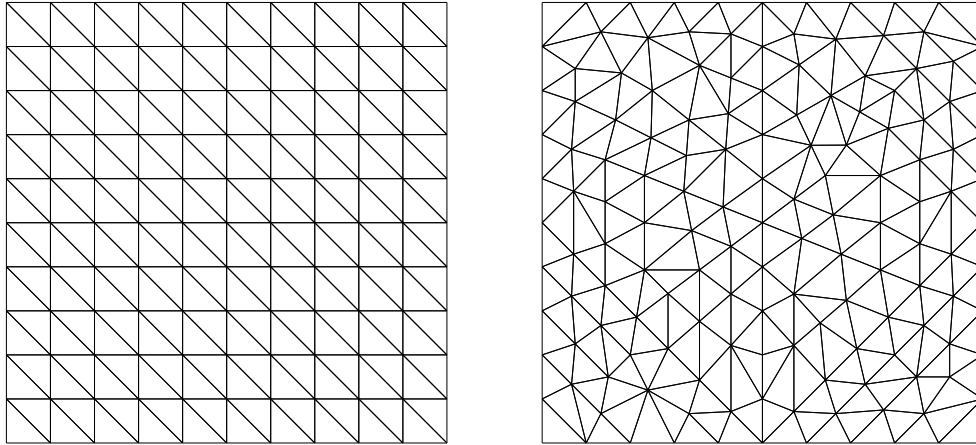


FIGURE 4.1: Structured *versus* unstructured mesh.

There are many available (open source) mesh generation software packages for both, 2D and 3D domains. For instance, the mesh on the left hand side in Fig. 4.1 is generated using MATLAB[®] source code, while the mesh on right hand side is designed in software package FreeFem++[®]. For creation of 2D unstructured meshes we decided to employ FreeFem++[®] because of its implementation simplicity. Previously, in order to find a mesh suitable for our real problem, we were tested a few more mesh generators, such as a library DistMesh() in MATLAB[®] environment and the package TRIANGLE[®] based on C++[®] programming language.

4.2 Discontinuous Galerkin formulation

As we stated before, we use DG discretization with respect to space variables only, whereas time remains continuous. This leads to a large system of ODEs, which can be solved numerically by a suitable ODE solver. This kind of approach is known as *a method of lines*. In particular, we will follow the next steps:

1. **Space discretization.** We divide a computational domain into elements and define a finite element space with discontinuous functions. This leads to a local scheme, where the exact solution is approximated on each element.
2. **Choice of numerical flux.** The global approximation to the exact solution is obtained by connecting all local solutions on the local elements via numerical flux. By clever choice of numerical flux we can afford a convergent numerical scheme. In particular, we shall choose a flux that solves Riemann problem (see Remark 4.2.1).
3. **Temporal integration.** Space discretization leads to a semi-discrete scheme that needs to be integrated in time. We use a low-storage explicit Runge-Kutta scheme.

In this section we focus on a scalar 2D conservation law whose associated Cauchy's problem is

$$\begin{aligned}\partial_t u + \nabla \cdot \mathbf{F}(u) &= 0, & (\mathbf{x}, t) &\in \Omega \times [0, T], \\ u(\mathbf{x}, t) &= g(\mathbf{x}, t), & (\mathbf{x}, t) &\in \partial\Omega \times [0, T], \\ u(\mathbf{x}, 0) &= h(\mathbf{x}), & \mathbf{x} &\in \Omega.\end{aligned}\tag{4.1}$$

Here $u = u(\mathbf{x}, t)$ is the unknown solution with $u : \Omega \times [0, T] \longrightarrow \mathbb{R}$, while $\mathbf{F} : \mathbb{R} \longrightarrow \mathbb{R}^{2 \times 1}$ is known flux function. Further, let the domain Ω be a bounded set with polygonal boundary $\partial\Omega$ and $\mathcal{T}_h = \{T_k\}_{k=1}^K$ be its conformal triangulation. In this case, we have a matching between physical domain Ω and computational domain Ω_h ,

$$\Omega \equiv \Omega_h = \bigcup_{k=1}^K T_k.$$

At this place, we take the occasion to introduce some function space terminology. Namely, let us recall on the Lebesgue space $L^2(\Omega)$, $\Omega \subset \mathbb{R}^n$ defined as a space of measurable functions $u : \Omega \longrightarrow \mathbb{R}$, such that $\int_{\Omega} u^2 dx < \infty$, equipped with norm

$$\|u\|_{L^2(\Omega)}^2 = \int_{\Omega} u^2 dx.$$

This is a Hilbert space with inner product

$$\langle u, v \rangle = \int_{\Omega} u v dx, \quad \langle u, u \rangle = \|u\|_{L^2(\Omega)}^2.$$

The well-known Cauchy-Schwartz inequality will be found useful

$$|\langle u, v \rangle| \leq \|u\|_{L^2(\Omega)} \|v\|_{L^2(\Omega)} \quad \text{for all } u, v \in L^2(\Omega).$$

Specially, on domain $\Omega_h = \bigcup_{k=1}^K T_k$ we define broken norm

$$\|u\|_{L^2(\Omega_h)}^2 = \sum_{k=1}^K \|u\|_{L^2(T_k)}^2, \quad \text{where} \quad \|u\|_{L^2(T_k)}^2 = \int_{T_k} u^2 dx.$$

We shall use the Sobolev space $H^p(\Omega)$ of functions such that all their weak partial derivatives of total order $\leq p$ belong to $L^2(\Omega)$. Its norm is given as

$$\|u\|_{H^p(\Omega)}^2 = \sum_{|\alpha|=0}^p \|u^{(\alpha)}\|_{L^2(\Omega)}^2,$$

where α denotes multi-index of length $|\alpha|$. The Sobolev broken norm reads as

$$\|u\|_{H^p(\Omega_h)}^2 = \sum_{k=1}^K \|u\|_{H^p(T_k)}^2, \quad \text{where} \quad \|u\|_{H^p(T_k)}^2 = \sum_{|\alpha|=0}^p \|u^{(\alpha)}\|_{L^2(T_k)}^2.$$

Finally, we will also use semi-norm defined on $H^p(\Omega)$,

$$|u|_{H^p(\Omega_h)}^2 = \sum_{k=1}^K |u|_{H^p(T_k)}^2, \quad \text{where} \quad |u|_{H^p(T_k)}^2 = \sum_{|\alpha|=p} \|u^{(\alpha)}\|_{L^2(T_k)}^2.$$

Any convergence shall be considered as a uniform. Lastly, we introduce the notation of average and jumps, respectively

$$\{u\} = \frac{u^- + u^+}{2}, \quad \llbracket u \rrbracket = \hat{\mathbf{n}}^- u^- - \hat{\mathbf{n}}^+ u^+, \quad \llbracket \mathbf{u} \rrbracket = \hat{\mathbf{n}}^- \cdot \mathbf{u}^- - \hat{\mathbf{n}}^+ \cdot \mathbf{u}^+.$$

4.2.1 Local approximation

Let us assume that we can approximate the exact solution of the Eq.(4.1) in the following way

$$u(\mathbf{x}, t) \simeq u_h(\mathbf{x}, t) = \bigoplus_{k=1}^K u_h^k(\mathbf{x}, t) \in V_h,$$

$$V_h := \{u_h \in L^2(\Omega) : u_h^k = u_h|_{T_k} \in V(T_k), \forall T_k \in \mathcal{T}_h\},$$

where V_h is the corresponding finite element space of discontinuous functions, while $V(T_k)$ is a local space¹. We set $V(T_k) = \mathcal{P}^N(T_k)$, which is the space of multivariate polynomials of total degree $N \in \mathbb{N}$ defined on element T_k .

In general, the basis functions of polynomial space come in essentially two forms, *nodal* and *modal* (sometimes called *a hierarchical*). A typical example for univariable modal basis is $\psi_n(x) = x^{n-1}$.

Nodal basis functions are known as Lagrangian interpolants ℓ_i and have the property that the basis coefficients are also function values at distinct interpolation points. It is worth mentioning that the uniqueness of Lagrange polynomial is ensured by using distinct interpolation points.

Using these two kinds of basis we express a local solution u_h^k on each element T_k as

$$u_h^k(\mathbf{x}, t) = \sum_{n=1}^{N_p} \hat{u}_n^k(t) \psi_n(\mathbf{x}) = \sum_{i=1}^{N_p} u_h^k(\mathbf{x}_i^k, t) \ell_i^k(\mathbf{x}). \quad (4.2)$$

Here \mathbf{x}_i^k $i = 1, \dots, N_p$ states for interpolation points whose number in 2D case takes value

$$N_p = \binom{N+2}{N}.$$

In order to simplify computations on elements, we introduce a mapping $\Theta : T_k \longrightarrow \mathcal{I}$ that transforms arbitrary triangle into the standard one²

$$\mathcal{I} = \{\mathbf{r} = (r, s) | r, s \geq -1, r + s \leq 0\}.$$

This yields to

$$u_h^k(\mathbf{r}, t) = \sum_{n=1}^{N_p} \hat{u}_n^k(t) \psi_n(\mathbf{r}) = \sum_{i=1}^{N_p} u_h^k(\mathbf{r}_i^k, t) \ell_i^k(\mathbf{r}).$$

Moreover, we can establish the connection between modal and nodal representation, *i.e.*, $\hat{\mathbf{u}} = (\hat{u}_1, \dots, \hat{u}_{N_p})^\top$ and $\mathbf{u} = (u(\mathbf{r}_1), \dots, u(\mathbf{r}_{N_p}))^\top$, using generalized Vandermonde matrix³ \mathcal{V} as follows

$$\mathcal{V} \hat{\mathbf{u}} = \mathbf{u}, \quad \mathcal{V}_{ij} = \phi_j(\mathbf{r}_i).$$

This allow us to equally use both bases in further theoretical investigations. Furthermore, by virtue of this relation we are capable to calculate 2D Lagrange polynomial for which an explicit expression does not exist.

There are many known interpolation nodes (see [6]), such as equidistant, Legendre–Gauss, Legendre–Gauss–Radau, Legendre–Gauss–Lobatto (LGL) nodes, *etc.* However, it can be shown that LGL nodes in 1D case lead to well-conditioned DG formulation [15]. These nodes are zeros of $(1 - r^2)P'_n(r)$, where P_n represents a *Legendre polynomial* of

¹Here, we have used notation of direct sum \oplus in order to emphasize that functions u_h^k , defined on T_k , are linearly independent functions.

²We are not going to write explicitly mapping Θ due to its technical complexity. We refer to [15] for more details.

³Sometimes in literature this matrix is called *an alternant matrix*.

order n . Formally, Legendre polynomial is a polynomial that solves a singular Sturm–Liouville problem, *i.e.*, ODE of type

$$\frac{d}{dr} \left((1-r^2) \frac{d}{dx} P_n(r) \right) + n(n+1) P_n(r) = 0.$$

Some of these polynomials are illustrated in Fig. 4.2.

For higher dimensions, LGL nodes are used to define suitable optimally distributed nodes that preserve stable and well-conditioned scheme. We will not go deep in details, thus we refer to [15].

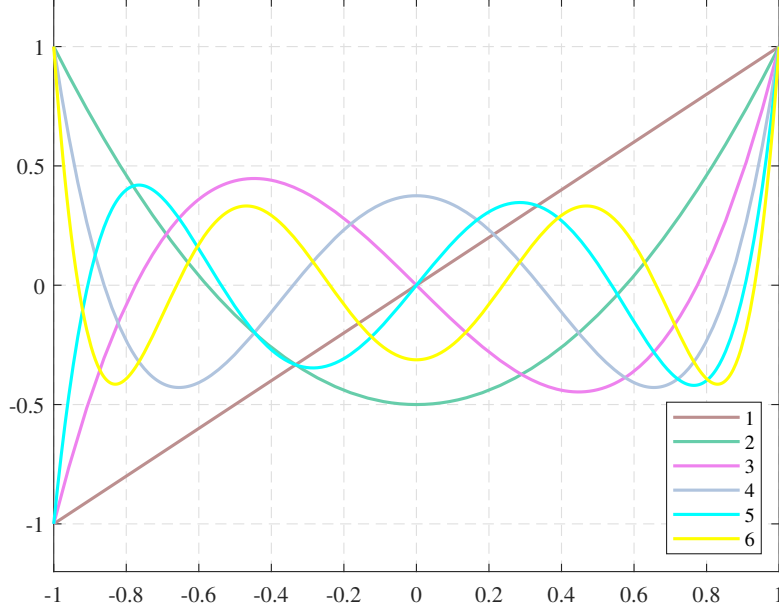


FIGURE 4.2: Illustration of the first six Legendre polynomials.

Further, we define a local residual \mathcal{R}_h^k on element T_k

$$\mathcal{R}_h^k := \partial_t u_h^k + \nabla \cdot \mathbf{F}(u_h^k).$$

In a spirit of FEM, we require that the local residual be L^2 -orthogonal to the piecewise polynomial test space (*e.g.* defined using nodal extension). In other words, the Galerkin orthogonality holds

$$\int_{T_k} \mathcal{R}_h^k \ell_h^k d\mathbf{x} = 0,$$

or more precisely,

$$\int_{T_k} (\partial_t u_h^k + \nabla \cdot \mathbf{F}(u_h^k)) \ell_h^k d\mathbf{x} = 0. \quad (4.3)$$

Let $\hat{\mathbf{n}}$ be outer unit normal pointing from T_k to adjacent element T_ℓ . Applying identity Eq.(2.5) and Gauss' theorem, Eq.(2.2), on Eq.(4.3) for each $k = 1, \dots, K$ we have

$$\int_{T_k} (\partial_t u_h^k \ell_i^k - \mathbf{F}(u_h^k) \cdot \nabla \ell_i^k) d\mathbf{x} = - \oint_{\partial T_k} \mathbf{F}(u_h^k) \cdot \hat{\mathbf{n}} \ell_i^k d\mathbf{x}. \quad (4.4)$$

Clearly, the integral from the right hand side in 3D is a surface integral while in 2D a line integral. In 1D, the analysis is simplified because the outer unit normal is either $+1$ on the right hand side of the element or -1 on the left hand side of the element, and an integration does not need to be performed.

4.2.2 Numerical flux

We seek to model physical flux \mathbf{F} by a so-called numerical flux \mathbf{F}^* which gives information about how the edge values of a local element T_k are connected to the edge values of a neighboring element T_ℓ . Thus, the numerical flux has to be a function depending on interior and exterior values of $u_h^k(\mathbf{x}_i)$, where $\mathbf{x}_i \in \partial T_k \cap \partial T_\ell$ (see Fig. 4.3). In particular, for a fixed time $t_0 \geq 0$ we define

$$\begin{aligned} u_h^{k,-}(\mathbf{x}, t_0) &= \lim_{\varepsilon \rightarrow 0^-} u_h^k(\mathbf{x} - \varepsilon \hat{\mathbf{n}}_{T_k}, t_0), \\ u_h^{k,+}(\mathbf{x}, t_0) &= \lim_{\varepsilon \rightarrow 0^+} u_h^k(\mathbf{x} - \varepsilon \hat{\mathbf{n}}_{T_\ell}, t_0), \end{aligned} \quad (4.5)$$

where we denoted the interior edge value of element T_k by $u_h^{k,-}$, whereas $u_h^{k,+}$ refers to the exterior values.

From now on, we will omit the superscript k in Eq.(4.5), because it will be clear from context which element is considered. To summarize, the notation ‘ $-$ ’ will refer to interior values of a local element, whereas ‘ $+$ ’ will be reserved to values that belongs to adjacent cells.

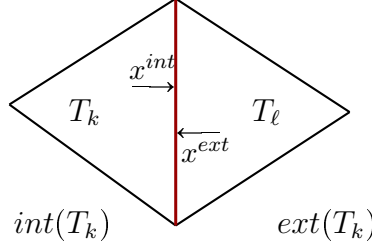


FIGURE 4.3: The illustration of the idea of numerical flux on the common edge (red) formed by two adjacent elements T_k and T_ℓ . If we consider the local element T_k and Eq.(4.5), the term *int* refers to superscript ‘ $-$ ’, while *ext* denotes ‘ $+$ ’.

In most considerations in this chapter we will use the numerical flux of the form

$$(au)^* = \{ \{ au \} \} + |a| \frac{1 - \alpha}{2} \llbracket u \rrbracket. \quad (4.6)$$

Specially, for $\alpha = 1$ we have *central flux*, while $\alpha = 0$ gives *upwind flux*.

REMARK 4.2.1 A Riemann problem consists of conservation law initial value problem together with piecewise constant initial data which has a single discontinuity in the domain of interest. It can be shown for the simple scalar case

$$\partial_t u + \lambda \partial_x u = 0, \quad x \in \Omega,$$

that the solution u has a discontinuity along a curve $x = \xi(t)$ when is fulfilled Rankine–Hugoniot condition $\llbracket f \rrbracket / \llbracket u \rrbracket = \lambda$, where $f = \lambda u$ and λ is the speed of the curve of discontinuity. This condition is simple consequence of conservation of u across the point of discontinuity. More about theory of Riemann problem can be found, e.g., in [12].

In our particular case, a Riemann problem occurs on each grid element. The numerical fluxes for linear conservation laws, as well as Maxwell’s equations in one space dimension that satisfy the Rankine–Hugoniot condition, are in details derived in [15]. Since the generalization is straightforward, in this work we will not do it explicitly.

Further, replacing in Eq.(4.4) physical flux with numerical one, we obtain the weak form

$$\int_{T_k} (\partial_t u_h^k \ell_i^k - \mathbf{F}(u_h^k) \cdot \nabla \ell_i^k) d\mathbf{x} = - \oint_{\partial T_k} \mathbf{F}^*(u_h^k) \cdot \hat{\mathbf{n}} \ell_i^k d\mathbf{x}, \quad (4.7)$$

and then, applying identity Eq.(2.5) and Gauss' theorem, Eq.(2.2), again, we get *the strong form*⁴ of the DG method

$$\int_{T_k} (\partial_t u_h^k + \nabla \cdot \mathbf{F}(u_h^k)) \ell_i^k d\mathbf{x} = - \oint_{\partial T_k} (\mathbf{F}(u_h^k) - \mathbf{F}^*(u_h^k)) \cdot \hat{\mathbf{n}} \ell_i^k d\mathbf{x}. \quad (4.8)$$

There are $K \times N_p$ equations to be solved for each component of the field corresponding to the values at the N_p grid points

$$\int_{T_k} (\partial_t u_h^k \ell_i^k - \mathbf{F}(u_h^k) \cdot \nabla \ell_i^k) \ell_j^k d\mathbf{x} = - \oint_{\partial T_k} \mathbf{F}^*(u_h^k) \cdot \hat{\mathbf{n}} \ell_i^k \ell_j^k d\mathbf{x}, \quad (4.9)$$

for $i, j = 1, \dots, N_p$. Next we define the element mass matrix \mathcal{M} and stiffness⁵ matrices $\nabla \mathcal{S}^k = (\mathcal{S}_x^k, \mathcal{S}_y^k)$ as follows

$$\begin{aligned} \mathcal{M}_{ij}^k &= \int_{T_k} \ell_i^k(\mathbf{x}) \ell_j^k(\mathbf{x}) d\mathbf{x} = J^k \int_{\mathcal{I}} \ell_i^k(\mathbf{r}) \ell_j^k(\mathbf{r}) d\mathbf{r} = J^k \mathcal{M}, \\ \mathcal{S}_{x,ij}^k &= \int_{T_k} \ell_i^k(\mathbf{x}) \partial_x \ell_j^k(\mathbf{x}) d\mathbf{x} = \int_{\mathcal{I}} \ell_i^k(\mathbf{r}) \partial_r \ell_j^k(\mathbf{r}) d\mathbf{r} = \mathcal{S}_{r,ij}, \\ \mathcal{S}_{y,ij}^k &= \int_{T_k} \ell_i^k(\mathbf{x}) \partial_y \ell_j^k(\mathbf{x}) d\mathbf{x} = \int_{\mathcal{I}} \ell_i^k(\mathbf{r}) \partial_s \ell_j^k(\mathbf{r}) d\mathbf{r} = \mathcal{S}_{s,ij}, \end{aligned}$$

where J^k is Jacobian of mapping Θ on element T^k . In these terms Eq.(4.9) becomes

$$\mathcal{M}^k \partial_t u_h^k - (\nabla \mathcal{S}^k)^\top \cdot \mathbf{F}_h^k = - \oint_{\partial T_k} \mathbf{F}^*(u_h^k) \cdot \hat{\mathbf{n}} \ell_i^k \ell_j^k d\mathbf{x}.$$

This directly lead us to local semi-discrete DG scheme

$$\frac{du_h^k}{dt} = \mathcal{L}_h(u_h^k, t), \quad (4.10)$$

where semi-discrete operator \mathcal{L}_h is given as⁶

$$\mathcal{L}_h(u_h^k, t) = (\mathcal{M}^k)^{-1} ((\nabla \mathcal{S}^k)^\top \cdot \mathbf{F}_h^k - \oint_{\partial T_k} \mathbf{F}^*(u_h^k) \cdot \hat{\mathbf{n}} \ell_i^k \ell_j^k d\mathbf{x}).$$

We solve the system of ODEs, Eqs.(4.10), using an explicit Runge–Kutta method (ERK). Generally, the main drawback of ERK methods is the conditional stability which requires strong limitation of the time step [2]. In next section we discuss more about this requirement. On the other hand, there are many different explicit and implicit ODE solvers which could also be applied at this place, but they will not be considered in this work.

⁴Notice that the strong form does not require smooth test functions. Specially, when a test function is delta function the scheme is called *collocation penalty method*.

⁵In classical finite element terminology, the discrete operator approximating the first derivative is called a *convection/advection matrix*.

⁶Note, the non-singularity of mass matrix \mathcal{M} follows from its structure. Namely, it can be straightforward shown that \mathcal{M} is symmetric and positive definite matrix.

4.2.3 Explicit Runge–Kutta method

Let us consider the (global) DG semi–discrete scheme

$$\frac{d\mathbf{u}_h}{dt} = \mathcal{L}_h(\mathbf{u}_h, t), \quad (4.11)$$

where \mathbf{u}_h is the vector of unknowns. The standard ERK method with s stages for Eq.(4.11) is defined via the recurrence formula

$$\begin{aligned} \mathbf{k}^{(1)} &= \mathcal{L}_h(\mathbf{u}_h^n, t^n), \\ \mathbf{k}^{(2)} &= \mathcal{L}_h(\mathbf{u}_h^n + \Delta t(a_{21}\mathbf{k}^{(1)}), t^n + c_2\Delta t), \\ \mathbf{k}^{(3)} &= \mathcal{L}_h(\mathbf{u}_h^n + \Delta t(a_{31}\mathbf{k}^{(1)} + a_{32}\mathbf{k}^{(2)}), t^n + c_3\Delta t), \\ &\vdots \\ \mathbf{k}^{(s)} &= \mathcal{L}_h(\mathbf{u}_h^n + \Delta t(a_{s1}\mathbf{k}^{(1)} + a_{s2}\mathbf{k}^{(2)} + \dots + a_{s,s-1}\mathbf{k}^{(s-1)}), t^n + c_s\Delta t), \\ \mathbf{u}_h^{n+1} &= \mathbf{u}_h^n + \Delta t \sum_{i=1}^s b_i \mathbf{k}^{(i)}, \end{aligned} \quad (4.12)$$

where Δt is step size. The matrix $\mathbf{A} = [a_{ij}]$ is called the Runge–Kutta matrix, while the \mathbf{b} and \mathbf{c} are known as the vectors of weights and nodes. These coefficients are arranged in a *Butcher tableau*⁷ (Table 4.1). In general, the stage s of an explicit Runge–Kutta

0					
c_2	a_{21}				
c_3	a_{31}	a_{32}			
\vdots	\vdots	\vdots	\ddots		
c_s	a_{s1}	a_{s2}	\dots	$a_{s,s-1}$	
	b_1	b_2	\dots	b_{s-1}	b_s

\mathbf{c}	\mathbf{A}
\mathbf{b}^\top	

TABLE 4.1: The Butcher tableau.

method with order p must satisfy $s \geq p$, and if $p \geq 5$, then $s \geq p + 1$ [2].

By careful look at procedure given by Eqs.(4.12), one can notice an obvious disadvantage during implementation of the classical ERK method when solving a large ODE system. Namely, ERK method requires s additional storage arrays, $\mathbf{k}^{(i)}$. Intending to avoid this, we use ‘a low–storage’ version of ERK method, or shortly, LSERK method.

Algorithm 1 LSERK(5, 4) & LSERK(14, 4)

```

 $\mathbf{p}^{(0)} = \mathbf{u}_h^n$ 
for  $i = 1, \dots, s$  where  $s = 5$  for LSERK(5, 4) or  $s = 14$  for LSERK(14, 4) do
     $\mathbf{k}^{(i)} = A_i^s \mathbf{k}^{(i-1)} + \Delta t \mathcal{L}_h(\mathbf{p}^{(i-1)}, t^n + C_i^s \Delta t)$ 
     $\mathbf{p}^{(i)} = \mathbf{p}^{(i-1)} + B_i^s \mathbf{k}^{(i)}$ 
end for
 $\mathbf{u}_h^{n+1} = \mathbf{p}^{(s)}$ 

```

One of celebrated LSERK methods is a forth order version with five stages introduced by Carpenter & Kennedy in [7]. The procedure is described in Algorithm 1, while its coefficients are given in Table 4.2. Application of LSERK(5, 4) diminish the memory

⁷In this context, the matrix \mathbf{A} is lower diagonal with zeros at diagonal entries. Otherwise, the Runge–Kutta method is implicit.

TABLE 4.2: Coefficients for the LSERK(5, 4) [7].

i	A_i^5	B_i^5	C_i^5
1	0	$\frac{1432997174477}{9575080441755}$	0
2	$-\frac{567301805773}{1357537059087}$	$\frac{5161836677717}{13612068292357}$	$\frac{1432997174477}{957080441755}$
3	$-\frac{2404267990393}{2016746695238}$	$\frac{1720146321549}{2090206949498}$	$\frac{2526269341429}{6820363962896}$
4	$-\frac{3550918686646}{2091501179385}$	$\frac{3134564353537}{4481467310338}$	$\frac{2006345519317}{3224310063776}$
5	$-\frac{1275806237668}{842570457699}$	$\frac{2277821191437}{14882151754819}$	$\frac{2802321613138}{2924317926251}$

TABLE 4.3: Coefficients for the LSERK(14, 4) method [27].

i	A_i^{14}	B_i^{14}	C_i^{14}
1	0.0000000000000000	0.0367762454319673	0.0000000000000000
2	-0.7188012108672410	0.3136296607553959	0.0367762454319673
3	-0.7785331173421570	0.1531848691869027	0.1249685262725025
4	-0.0053282796654044	0.0030097086818182	0.2446177702277698
5	-0.8552979934029281	0.3326293790646110	0.2476149531070420
6	-3.9564138245774565	0.2440251405350864	0.2969311120382472
7	-1.5780575380587385	0.3718879239592277	0.3978149645802642
8	-2.0837094552574054	0.6204126221582444	0.5270854589440328
9	-0.7483334182761610	0.1524043173028741	0.6981269994175695
10	-0.7032861106563359	0.0760894927419266	0.8190890835352128
11	0.0013917096117681	0.0077604214040978	0.8527059887098624
12	-0.0932075369637460	0.0024647284755382	0.8604711817462826
13	-0.9514200470875948	0.0780348340049386	0.8627060376969976
14	-7.1151571693922548	5.5059777270269628	0.8734213127600976

requirements related to arrays storage. In fact, only one additional array is needed to be stored. From the other side, due to presence of fifth stage, additional function evaluation have to be performed.

One of alternative approach to LSERK(5, 4) is version that uses 14 stages instead of five, proposed by Niegemann et al. in [27], the LSERK(14, 4). The method is presented in Algorithm 1, while its complementing coefficients can be found in Table 4.3. Here an extra storage array is also required. Unlike to the previous low storage method, this comes with an extra cost of ten additional functions, due to existence of ten more stages. However, it will be shown in Section 4.3.2 that LSERK(14, 4) allows a large stable time-step Δt .

The connection between coefficients in Tables 4.2–4.3 and Butcher coefficients given in Table 4.1 depending on number of stages s that are used, is the following

$$a_{ij} = \begin{cases} A_{j+1}^s a_{i,j+1} + B_j^s & j < i - 1, \\ B_j^s & j = i - 1, \\ 0 & \text{otherwise,} \end{cases}$$

$$b_i = \begin{cases} A_{i+1}^s b_{i+1} + B_i^s & i < s, \\ B_i^s & i = s. \end{cases}$$

4.3 Theoretical Validation

In this section we will justify some DG's properties essential to any numerical method. With minimal loss of generality, we shall focus on the one-dimensional case. Therefore, let us consider the 1D Cauchy problem with symmetric diagonalizable $m \times m$ matrix $\mathcal{A} = \mathcal{A}(x, t)$ (i.e., a hyperbolic system of PDEs) on $\Omega = [L, R]$

$$\frac{\partial \mathbf{u}}{\partial t} + \mathcal{A} \frac{\partial \mathbf{u}}{\partial x} = \mathbf{0}, \quad x \in \Omega, t \geq 0. \quad (4.13)$$

DEFINITION 4.3.1 *A problem is well posed if it admits a unique solution \mathbf{u} and there exist $\alpha, C \geq 0$ such that*

$$\|\mathbf{u}(t)\|_{L^2(\Omega)} \leq C e^{\alpha t} \|\mathbf{u}(0)\|_{L^2(\Omega)}. \quad (4.14)$$

Intuitively, Eq.(4.14) means that solution must not be sensitive on changes in initial data. We assume that Eq.(4.13) is completed with initial and boundary conditions such that the wellposedness is fulfilled.

Let \mathbf{u}_h be a piecewise N -th-order polynomial approximation of \mathbf{u} and \mathcal{L}_h be a discrete approximation of continuous operator $\mathcal{A}\partial_x$ such that holds

$$\frac{d\mathbf{u}_h}{dt} + \mathcal{L}_h \mathbf{u}_h = \mathbf{0}. \quad (4.15)$$

Substituting exact solution \mathbf{u} in Eq.(4.15) we obtain a *truncation error* $\mathcal{T}(\mathbf{u})$, which represents the error committed during discretization of the continuous operator

$$\frac{d\mathbf{u}}{dt} + \mathcal{L}_h \mathbf{u} = \mathcal{T}(\mathbf{u}). \quad (4.16)$$

Considering the (global) error

$$\mathbf{e}_h = \mathbf{u} - \mathbf{u}_h$$

in Eq.(4.16) and using Eq.(4.15) we get ODE with respect to time

$$\frac{d\mathbf{e}_h}{dt} + \mathcal{L}_h \mathbf{e}_h = \mathcal{T}(\mathbf{u})$$

whose exact solution (obtained using *e.g.* variation of constants) is

$$\mathbf{e}_h(t) - e^{-\mathcal{L}_h t} \mathbf{e}_h(0) = \int_0^t e^{\mathcal{L}_h(s-t)} \mathcal{T}(\mathbf{u}(s)) ds. \quad (4.17)$$

Integrating Eq.(4.17) over the elements T_k and summing up, afterwards using triangle inequality for norm and integral, we reach to

$$\|\mathbf{e}_h(t)\|_{L^2(\Omega_h)} \leq \|e^{-\mathcal{L}_h t} \mathbf{e}_h(0)\|_{L^2(\Omega_h)} + \int_0^t \|e^{-\mathcal{L}_h(s-t)}\|_{L^2(\Omega_h)} \|\mathcal{T}(\mathbf{u}(s))\|_{L^2(\Omega_h)} ds \quad (4.18)$$

According to Lax–Richtmyer equivalence theorem [20], to have a *convergent* well posed linear problem it is enough to ensure *consistency* and *stability*. The consistency is described by approximation of functions and operators

$$\lim_{dof \rightarrow \infty} \|\mathbf{e}_h(0)\|_{L^2(\Omega_h)} = 0 \quad \text{and} \quad \lim_{dof \rightarrow \infty} \|\mathcal{T}(\mathbf{u}(t))\|_{L^2(\Omega_h)} = 0,$$

while stability requires

$$\lim_{dof \rightarrow \infty} \|e^{-\mathcal{L}_h t}\|_{L^2(\Omega_h)} \leq C_h e^{\alpha t}.$$

Note a bond between stability and wellposedness; one can interpret the stability as wellposedness of matrix exponential problem ($\mathbf{u}(t) = e^{-\mathcal{L}_h t}$ in Eq.(4.14)) regardless of grid or polynomial order refinements (see Remark 4.3.1).

REMARK 4.3.1 In the last limits we introduced a term ‘dof’ – degree of freedom, which refers to possibility to achieve the convergence in different ways. Namely, we can either reduce the element size – h -convergence or increase the order of polynomial – p -convergence or even make a combination of both – hp -convergence.

4.3.1 Consistency

Within this subsection we shall determine the conditions under which we can expect a consistency of DG semi-discrete scheme.

Unlike 2D case where the mapping Θ transformed triangles, in 1D case Θ maps arbitrary subinterval into $\mathcal{I} = [-1, 1]$. In particular, if $x \in T_k = [x_\ell^k, x_r^k]$, then

$$x(r) = x_\ell^k + \frac{1+r}{2}h^k, \quad \text{where} \quad h^k = x_r^k - x_\ell^k \quad \text{and} \quad r \in \mathcal{I}.$$

We assume, without loss of generality, that all cells have the same length h . Further, we define on \mathcal{I}

$$v(r) = u(hx) = u(x). \quad (4.19)$$

In the case of order refinement (see Remark 4.3.1), we give the result whose proof is technical and can be found in [5, Th.4.7].

THEOREM 4.3.1 Let $v \in H^p(\mathcal{I})$, $p > 1/2$, and v_h be its polynomial interpolation of order N . Then

$$\|v - v_h\|_{H^q(\mathcal{I})} \leq N^{2q-p+1/2} |v|_{H^p(\mathcal{I})},$$

where $0 \leq q \leq p$.

Let us now focus on consistency under element refinement. Unlike previous case, here we are capable to reveal an error estimate for u rather than v . This we will be proposed in the theorem that follows. Before that we give a lemma from interpolation theory (see lemmata 4.2.–4.4 in [15]).

LEMMA 4.3.1 Let $v \in H^p(\mathcal{I})$, $p \geq 1$, and v_h be its polynomial interpolation of order N . Then

$$\|v^{(q)} - v_h^{(q)}\|_{H^0(\mathcal{I})} \leq N^{2q-p} |v|_{H^p(\mathcal{I})},$$

where $\sigma = \min\{N+1, p\}$ and $q \leq p$.

THEOREM 4.3.2 (Th.4.7. in [15]) Let $u \in H^p(T_k)$ and u_h be its piecewise polynomial approximation of order N . Then

$$\|u - u_h\|_{H^q(\Omega_h)} \leq Ch^{\sigma-q} |u|_{H^\sigma(\Omega_h)},$$

for $0 \leq q \leq \sigma$, where $\sigma = \min\{N+1, p\}$.

PROOF. Using the substitution from the beginning of this subsection Eq.(4.19) we easily find relation between u and v in norms of Sobolev spaces

$$\begin{aligned} |v|_{H^q(\mathcal{I})}^2 &= \int_{\mathcal{I}} (v^{(q)})^2 dr = \int_{T_k} h^{2q-1} (u^{(q)})^2 dx = h^{2q-1} |u|_{H^q(T_k)}^2, \\ \|u\|_{H^q(T_k)}^2 &= \sum_{p=0}^q |u|_{H^p(T_k)}^2 = \sum_{p=0}^q h^{1-2p} |v|_{H^p(\mathcal{I})}^2 \leq h^{1-2p} \|v\|_{H^q(\mathcal{I})}^2. \end{aligned}$$

Combining these two estimates with Lemma 4.3.1 we obtain

$$\|u - u_h\|_{H^q(T_k)}^2 \leq h^{1-2q} \|v - v_h\|_{H^q(\mathcal{I})}^2 \leq h^{1-2q} |v|_{H^\sigma(\mathcal{I})}^2 \leq h^{2\sigma-2q} |u|_{H^\sigma(T_k)}^2.$$

Finally, summing up the last expression over all elements, the result yields. \square

The next theorem represents a generalization of the previous one. Namely, for more general grids where the length h is chosen to be the maximal subinterval length, we have the following result.

THEOREM 4.3.3 (TH.4.8. IN [15]) *Let $u \in H^p(T_k)$, $p > 1/2$, and u_h be its piecewise polynomial approximation of order N . Then*

$$\|u - u_h\|_{H^q(\Omega_h)} \leq C \frac{h^{\sigma-q}}{N^{p-2q-1/2}} |u|_{H^\sigma(\Omega_h)},$$

for $0 \leq q \leq \sigma$, where $\sigma = \min\{N+1, p\}$.

4.3.2 Stability

We continue with the analysis of the Cauchy problem Eq.(4.13) with the inspection of the stability condition. A semi-discrete scheme that corresponds to its i -th component of Eq.(4.13)

$$\partial_t u_i + (\mathcal{A} \partial_x u)_i = \partial_t u_i + \sum_{j=1}^m \mathcal{A}_{ij} \partial_x u_j = 0$$

is given as

$$\mathcal{M}^k \frac{du_{i,h}^k}{dt} + \sum_{j=1}^m \mathcal{A}_{ij} \mathcal{S} u_{j,h}^k = \oint_{\partial T_k} \hat{\mathbf{n}} \cdot \left(\sum_{j=1}^m \mathcal{A}_{ij} u_j \right)^* dx. \quad (4.20)$$

If we suppose that the matrix \mathcal{A} is uniformly diagonalizable, there exists a matrix \mathcal{R} such that

$$\mathcal{A} = \mathcal{R} \Lambda \mathcal{R}^{-1} \quad \text{and} \quad \|\mathcal{R}\|_{L^2(\Omega_h)} \|\mathcal{R}^{-1}\|_{L^2(\Omega_h)} \leq C_h.$$

This gives rise to introduce the substitution $\mathbf{v} = \mathcal{R}^{-1} \mathbf{u}$ in Eq.(4.13). Consequently, the Eq.(4.20) becomes

$$\mathcal{M}^k \frac{dv_{i,h}^k}{dt} + \Lambda_{ii} \mathcal{S} v_{i,h}^k = \int_{\partial T_k} \hat{\mathbf{n}} \cdot (\Lambda_{ii} v_i)^* dx. \quad (4.21)$$

One can conclude that the semi-discrete scheme Eq.(4.21) coincides with scheme for the problem of type

$$\frac{\partial u}{\partial t} + a \frac{\partial u}{\partial x} = 0, \quad (4.22)$$

whose stability will be explained at the very end of this subsection.

Finally, stability of the scheme Eq.(4.20) yields from

$$\begin{aligned} \|\mathbf{u}_h(t)\|_{L^2(\Omega_h)}^2 &= \|\mathcal{R} \mathbf{v}_h(t)\|_{L^2(\Omega_h)}^2 \\ &\leq \|\mathcal{R}\|_{L^2(\Omega_h)}^2 \|\mathbf{v}_h(t)\|_{L^2(\Omega_h)}^2 \\ &\leq \|\mathcal{R}\|_{L^2(\Omega_h)}^2 e^{\alpha_h t} \|\mathbf{v}_h(0)\|_{L^2(\Omega_h)}^2 \\ &\leq \|\mathcal{R}\|_{L^2(\Omega_h)}^2 e^{\alpha_h t} \|\mathcal{R}^{-1} \mathbf{u}_h(0)\|_{L^2(\Omega_h)}^2 \\ &\leq \|\mathcal{R}\|_{L^2(\Omega_h)} \|\mathcal{R}^{-1}\|_{L^2(\Omega_h)} e^{\alpha_h t} \|\mathbf{u}_h(0)\|_{L^2(\Omega_h)}^2 \\ &\leq C_h e^{\alpha_h t} \|\mathbf{u}_h(0)\|_{L^2(\Omega_h)}^2, \end{aligned}$$

where we used uniform diagonalization of matrix \mathcal{A} and stability for scalar case (see in the sequel).

Stability of semi-discrete scheme for scalar 1D conservation law

Let us recall the local nodal expression on element $T_k = [x_\ell^k, x_r^k]$

$$u_h^k(x, t) = \sum_{i=1}^{N_p} u_h^k(x_i^k, t) \ell_i^k(x) = (\mathbf{u}_h^k)^\top \boldsymbol{\ell}^k(x),$$

where $\mathbf{u}_h^k = (u_1^k, \dots, u_{N_p}^k)^\top$ with $u_i^k := u_h^k(x_i^k, t)$ is the vector of the local nodal solution and $\boldsymbol{\ell}^k(x) = (\ell_1^k(x), \dots, \ell_{N_p}^k(x))^\top$ is vector of Lagrange polynomials. A local strong semi-discrete scheme for the PDE Eq.(4.22) has the form

$$\mathcal{M}^k \frac{d\mathbf{u}_h^k}{dt} + \mathcal{S}^k(a\mathbf{u}_h^k) = \left[\boldsymbol{\ell}^k(x)(au_h^k - (au_h)^*) \right]_{x_\ell^k}^{x_r^k}, \quad (4.23)$$

where discrete operators are defined as

$$\mathcal{M}_{ij}^k = \langle \ell_i^k, \ell_j^k \rangle \quad \text{and} \quad \mathcal{S}_{ij}^k = \left\langle \ell_i^k, \frac{d\ell_j^k}{dx} \right\rangle.$$

Before we dive into the derivation of energy estimate, note that

$$\begin{aligned} (\mathbf{u}_h^k)^\top \mathcal{M}^k \mathbf{u}_h^k &= \sum_{i=1}^{N_p} u_h^k(x_i^k, t) (\mathcal{M}^k \mathbf{u}_h^k)_i \\ &= \sum_{i=1}^{N_p} u_h^k(x_i^k, t) \sum_{j=1}^{N_p} \mathcal{M}_{ij}^k u_h^k(x_j^k, t) \\ &= \sum_{i=1}^{N_p} u_h^k(x_i^k, t) \sum_{j=1}^{N_p} \left(\int_{T_k} \ell_i^k(x) \ell_j^k(x) dx \right) u_h^k(x_j^k, t) \\ &= \int_{T_k} \left(\sum_{i=1}^{N_p} u_h^k(x_i^k, t) \ell_i^k(x) \right) \left(\sum_{j=1}^{N_p} u_h^k(x_j^k, t) \ell_j^k(x) \right) dx \\ &= \|u_h^k\|_{L^2(T_k)}^2, \end{aligned}$$

and similarly

$$(\mathbf{u}_h^k)^\top \mathcal{S}^k \mathbf{u}_h^k = \frac{1}{2} [(u_h^k)^2]_{x_\ell^k}^{x_r^k}.$$

This clarifies why multiplication by \mathbf{u}_h^k the Eq.(4.23) from the left hand side gives

$$\begin{aligned} \frac{d}{dt} \|u_h^k\|_{L^2(T_k)}^2 &= -a [(u_h^k)^2]_{x_\ell^k}^{x_r^k} + 2 [u_h^k (au_h^k - (au)^*)]_{x_\ell^k}^{x_r^k} \\ &= [a(u_h^k)^2 - 2u_h^k (au)^*]_{x_\ell^k}^{x_r^k}. \end{aligned} \quad (4.24)$$

Stability of hyperbolic system is characterized by non-increasing energy. In other words, it is enough to show

$$\sum_{k=1}^K \frac{d}{dt} \|u_h^k\|_{L^2(T_k)}^2 = \frac{d}{dt} \|u_h\|_{L^2(\Omega_h)}^2 \leq 0. \quad (4.25)$$

Due to presence of degrees of freedom, we are capable to force upon additional conditions. Namely, we take the numerical flux declared in Eq.(4.6). Further, we assume $a > 0$ and $(au)(L) = 0$ and $(au)(R) = au_h(x_r^K)$.

Summing over the elements Eq.(4.25) and doing some algebraic manipulations we obtain

$$\frac{d}{dt} \|u_h\|_{L^2(\Omega_h)}^2 = \underbrace{-|a|(1-\alpha) \sum_{k=1}^{K-1} \|u_h^k(x_r^k)\|^2}_{\text{Interior interfaces}} - \underbrace{(1-\alpha)a(u_h^1(x_\ell^1))^2}_{\text{Left BC}} - \underbrace{a(u_h^K(x_\ell^K))^2}_{\text{Right BC}}.$$

Clearly, under current assumptions, the stability is ensured by $0 \leq \alpha \leq 1$. Nevertheless, there are other approaches [15] motivated by the physical nature of the considered problem that also provide non-increasing energy.

4.3.3 Discrete Stability

So far we have been focused on the convergence analysis of semi-discrete scheme, due to the method of lines approach. In this subsection we shall give a necessary condition for stability of fully discrete RKDG scheme.

In order to define step size Δt that provides a stable temporal scheme, we shall first consider the test ODE

$$u_t = \lambda u, \quad u(0) = 1, \quad (4.26)$$

where $\lambda \in \mathbb{C}$, and whose exact solution is $u(t) = e^{\lambda t}$. Clearly, to ensure stability, the quantity $|\lambda t|$ must be bounded at infinity, when $t \rightarrow \infty$.

Let $t^0 < t^1 < \dots < t^{N-1} < t^N$, $N \in \mathbb{N}$ be a uniform grid of the time interval $[0, T]$, such that $t^n = n\Delta t$. The analytic solution at grid point is given as

$$\begin{aligned} u(t^{n+1}) &= e^{\lambda(n+1)\Delta t} \\ &= e^{\lambda\Delta t} u(t^n). \end{aligned}$$

Let u^n be an approximation of the analytical solution $u(t^n)$, then

$$u^{n+1} = R(\lambda\Delta t)u^n,$$

where

$$R(\lambda\Delta t) \approx e^{\lambda\Delta t} \quad (4.27)$$

states for an approximation of exponential function.

DEFINITION 4.3.2 *The function R in Eq.(4.27) is called the stability function of the corresponding numerical scheme.*

Usually, the function R is a polynomial function or a rational function whose numerator and denominator are both polynomial functions.

DEFINITION 4.3.3 *Let R be the stability function. Then, the stability region of the corresponding numerical scheme is defined as*

$$\mathcal{S} = \{z \in \mathbb{C} : |R(z)| \leq 1\}.$$

It can be shown [2] that the stability function of s -stage ERK of arbitrary order p is given as

$$R(z) = 1 + z + \frac{z^2}{2!} + \frac{z^3}{3!} + \dots + \frac{z^p}{p!} + \sum_{j=p+1}^s z^j \mathbf{b}^\top \mathbf{A}^{j-1} \mathbf{1},$$

where $\mathbf{1} = (1, 1, \dots, 1)^\top \in \mathbb{R}^s$. This function is used for the plot in Fig. 4.4.

Let us return back to main problem, the discrete DG scheme

$$\frac{d\mathbf{u}_h}{dt} + \mathcal{L}_h \mathbf{u}_h = \mathbf{0},$$

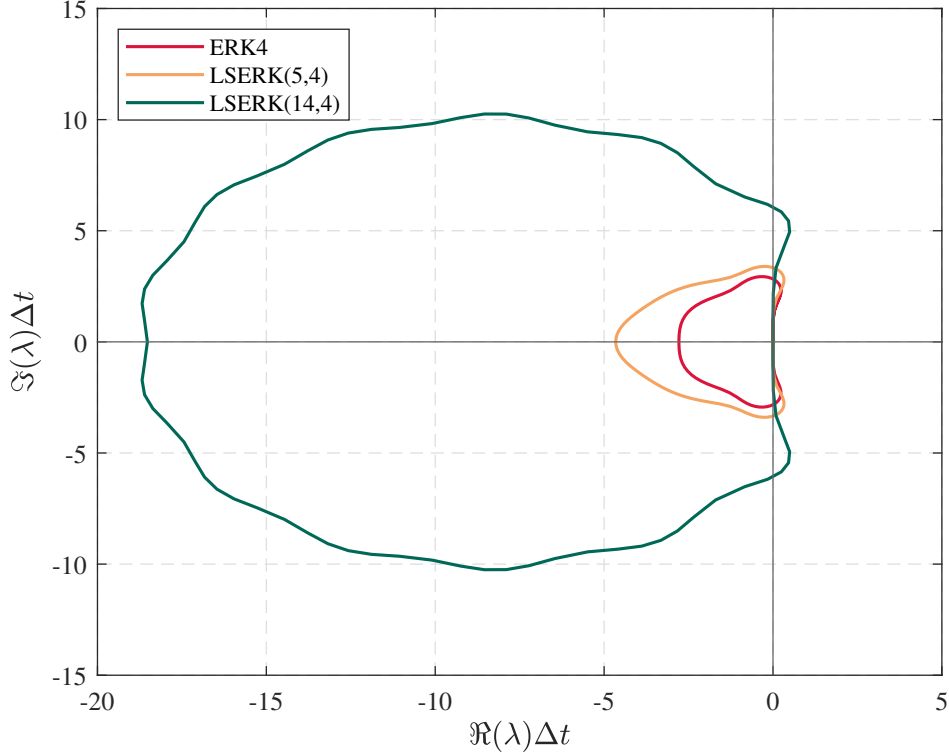


FIGURE 4.4: Stability regions of fourth-order Runge-Kutta methods: ERK4, LSERK(5,4) and LSERK(14,4).

where $\mathcal{L}_h \approx \partial_x a$. The idea is to choose Δt sufficiently small such that entire spectrum of \mathcal{L}_h fits in stability region of the temporal scheme [15].

From semi-discrete weak form we conclude that

$$\mathcal{L}_h = \frac{2a}{h} \mathcal{M}^{-1} [\mathcal{S} - \mathcal{E}], \quad (4.28)$$

where \mathcal{E} denotes a matrix whose entries are zeros except the first and the last diagonal entry. In Figs. 4.5–4.8, we consider periodic boundary conditions in combination with different choices of numerical flux (*i.e.* central, partly upwind and fully upwind flux) for equation $\partial_t u + a \partial_x u = 0$, with $a = 1$ on interval $[0, 1]$ broken into K equal subinterval. These figures depict sets of eigenvalues λ_N of discrete operator \mathcal{L}_h from Eq.(4.28).

Comparing stability regions of three Runge-Kutta methods whose stability regions are plotted in Fig. 4.4 with spectrum illustrated in Figs. 4.5–4.8, it can be concluded that we may always find Δt sufficiently small such that $\Delta t \lambda_N$ fits in stability region at least of RK method that posses the widest contour, LSERK(14,4). This gives necessary stability condition, whereas the sufficient one is quite demanding and here will not be considered (see *e.g.* [19]).

Special accent goes to the cases that include increasing of polynomial order, *e.g.* Figs. 4.7 and 4.8. As can be seen, the spectrum get significantly spread. This gives rise to choose time-step such that the eigenvalue with maximal amplitude stays bounded from above. In fact, it can be experimentally shown [15] that the next estimate preserves stability of temporal scheme

$$\max(|\lambda_N|) \leq \frac{3}{2} \max_i (\Delta r_i)^{-1}, \quad (4.29)$$

where Δr_i is distance between to adjacent nodes on \mathcal{I} .

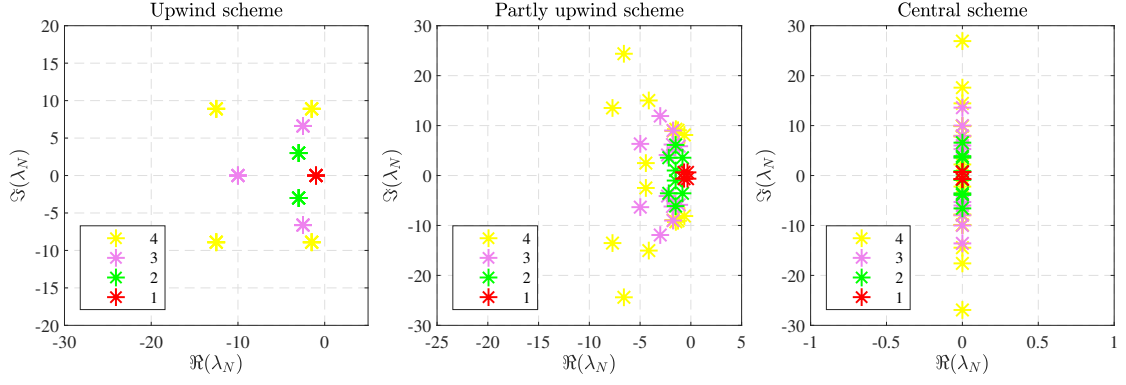


FIGURE 4.5: Spectrum of operator \mathcal{L}_h for $K = 4$ and $N = 1, 2, 3, 4$.

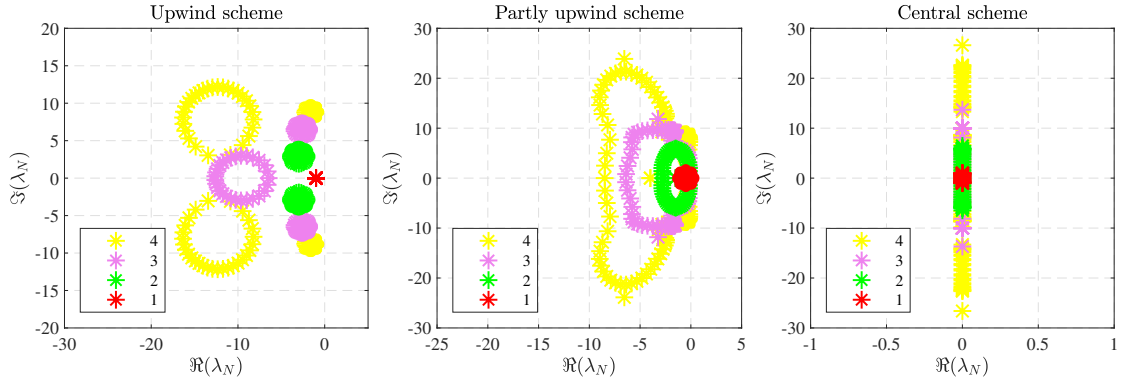


FIGURE 4.6: Spectrum of operator \mathcal{L}_h for $K = 29$ and $N = 1, 2, 3, 4$.

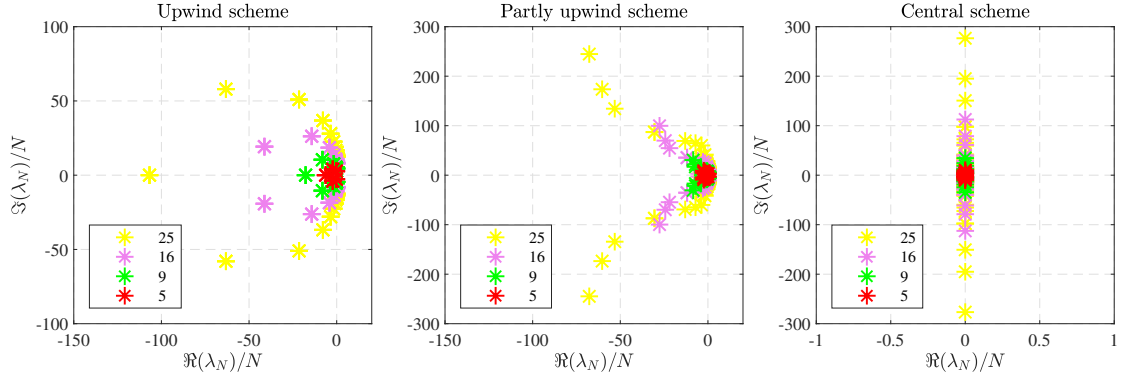


FIGURE 4.7: Spectrum of operator \mathcal{L}_h for $K = 4$ and $N = 5, 9, 16, 25$.

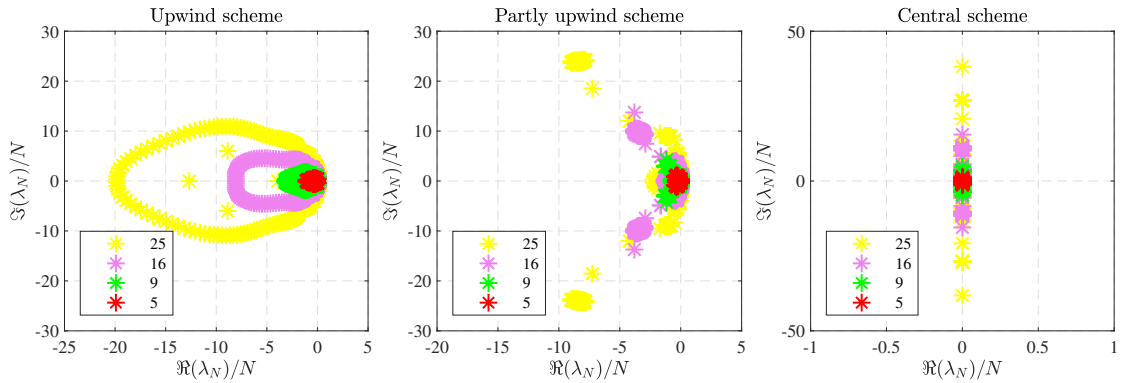


FIGURE 4.8: Spectrum of operator \mathcal{L}_h for $K = 29$ and $N = 5, 9, 16, 25$. See text for discussion.

We introduce a CFL (Courant–Friedrics–Lewy)–like stability restrictions on the time–step

$$\Delta t \leqslant C(N) \min(\Delta x).$$

More precisely, for problem $\partial_t u + a \partial_x u = 0$, whose length of elements is h^k (on Ω) and node spacing is $\Delta_i r$ (on \mathcal{I}), the CFL condition for RKDG is given as

$$\Delta t \leqslant C \frac{1}{|a|} \min_{k,i} \frac{h^k}{2} \Delta_i r. \quad (4.30)$$

For systems $\partial_t \mathbf{u} + \mathcal{A} \partial_x \mathbf{u} = \mathbf{0}$, the generalization of Eq.(4.30) takes form

$$\Delta t \leqslant C \frac{1}{\max |\lambda(\mathcal{A})|} \min_{k,i} \frac{h^k}{2} \Delta_i r. \quad (4.31)$$

Chapter 5

Numerical Results

This chapter is devoted to visualization of the theoretical work previously exposed. In that purpose, codes from Hesthaven's and Warburton's book [15] for TM-mode we adapted in order to consider not just the TE-mode but also to include other characteristics specific to our problem. The notation from previous chapter is inherited and upgraded when needed. The theory proposed in Chapter 4 and Subsection 2.2.1 allows us to quickly recover a semi-discrete DG schemes for 2D Maxwell's curl-equations in Section 5.1. Afterwards, in Section 5.2 we perform several numerical experiments in order to justify reliability of the method applied on our specific problem. More precisely, we investigate stability of the method using spectral properties of DG operator, and the convergence, both in space and in time, with the help of a numerical example.

Finally, the Section 5.3 is dedicated to the main purpose of this work. Namely, we comeback to the application presented in the beginning of this document and consider the numerical simulation of light scattering in the human's cornea aiming to mimicking the OCT imaging system. A two-dimensional model of backscattered light intensity is proposed and its time evolution is considered both for healthy and pathological tissues. In the very end of chapter, an analysis of the amount of scattered light during propagation is presented.

5.1 DG Formulation for Maxwell's equations

We start by formulating the conservative form of TE-mode Maxwell's equations in 2D (3.6), *i.e.*,

$$\mathbf{Q} \partial_t \mathbf{u} + \nabla \cdot \mathbf{F}(\mathbf{u}) = \mathbf{0} \quad \text{on} \quad \Omega \times [0, T], \quad (5.1)$$

where the state vector is given as $\mathbf{u} = (E_x, E_y, H_z)^\top$, whereas the material matrix \mathbf{Q} and the flux vector \mathbf{F} are defined as

$$\mathbf{Q} = \begin{pmatrix} \varepsilon & \mathbf{0} \\ \mathbf{0}^\top & \mu \end{pmatrix}, \quad \varepsilon = \begin{pmatrix} \varepsilon_{xx} & \varepsilon_{xy} \\ \varepsilon_{yx} & \varepsilon_{yy} \end{pmatrix}, \quad \text{and} \quad \mathbf{F}(\mathbf{u}) = \begin{pmatrix} 0 & -H_z \\ H_z & 0 \\ E_y & -E_x \end{pmatrix}.$$

As usual, $\mathbf{u}_h = (E_h^x, E_h^y, H_h^z)$ is the approximate solution of Eq.(5.1) whose component fields belong to the space V_h (presented in Subsection 4.2.1),

$$\mathbf{u}_h = \bigoplus_{k=1}^K \mathbf{u}_h^k \in V_h^3, \quad \text{where} \quad \mathbf{u}_h^k(\mathbf{x}, t) = \sum_{i=1}^{N_p} \mathbf{u}_h^k(\mathbf{x}_i^k, t) \ell_i^k(\mathbf{x}).$$

Repeating the similar procedure as in Chapter 4, we can easily obtain the strong form,

$$\int_{T_k} (\mathbf{Q} \partial_t \mathbf{u}_h^k + \nabla \cdot \mathbf{F}(\mathbf{u}_h^k)) \ell_i^k d\mathbf{x} = \oint_{\partial T_k} \hat{\mathbf{n}} \cdot (\mathbf{F} - \mathbf{F}^*) \ell_i^k d\mathbf{x}. \quad (5.2)$$

In the remaining of the work it will be handy to use the following notation for the field discontinuities across the element's boundaries

$$[u] = u^- - u^+ = \hat{\mathbf{n}} \cdot \llbracket u \rrbracket.$$

We consider the numerical flux that corresponds to an anisotropic medium [18],

$$\hat{\mathbf{n}} \cdot (\mathbf{F} - \mathbf{F}^*) = \begin{pmatrix} \frac{-n_y}{Z^+ + Z^-} (Z^+[H_z] - \alpha(n_x[E_y] - n_y[E_x])) \\ \frac{n_x}{Z^+ + Z^-} (Z^+[H_z] - \alpha(n_x[E_y] - n_y[E_x])) \\ \frac{1}{Y^+ + Y^-} (Y^+(n_x[E_y] - n_y[E_x]) - \alpha[H_z]) \end{pmatrix}, \quad (5.3)$$

with the upwinding parameter $\alpha \in [0, 1]$. The parameter α regulates the wave dissipation¹, *i.e.* $\alpha = 0$ yields to non-dissipative central flux, while $\alpha = 1$ adds extra dissipative terms that result the upwind flux. We may say that α brings an artificial dissipation in system.

The impedance Z and conductance Y are related by

$$Z^\pm = \frac{1}{Y^\pm} = \mu^\pm c^\pm, \quad c^\pm = \sqrt{\frac{\hat{\mathbf{n}}^\top \boldsymbol{\varepsilon}^\pm \hat{\mathbf{n}}}{\mu^\pm \det(\boldsymbol{\varepsilon}^\pm)}}.$$

We consider the boundary conditions imposed by the numerical flux, due to its crucial role in DG method which manifests in the exchange of the information between cells.

Using the mirror principle, we set the differences at all boundary points for PEC boundary conditions as

$$[E_x] = 2E_x^-, \quad [E_y] = 2E_y^-, \quad [H_z] = 0. \quad (5.4)$$

Similarly, the jumps at the boundary for PMC are

$$[E_x] = 0, \quad [E_y] = 0, \quad [H_z] = 2H_z^-. \quad (5.5)$$

The SM-ABC are implemented such that incoming flux at boundary is zero. For the upwind flux this means [1]

$$Z^- H_z^+ = n_x E_y^+ - n_y E_x^+ \quad \Leftrightarrow \quad H_z^+ = Y^-(n_x E_y^+ - n_y E_x^+). \quad (5.6)$$

When the central flux is used, we have

$$Z^- H_z^+ = n_x E_y^- - n_y E_x^- \quad \Leftrightarrow \quad H_z^+ = Y^-(n_x E_y^- - n_y E_x^-). \quad (5.7)$$

Assuming $\alpha = 1$ in Eq.(5.3) we may merge the conditions Eqs.(5.6)–(5.7) in the single condition

$$[E_x] = E_x^-, \quad [E_y] = E_y^-, \quad [H_z] = H_z^-. \quad (5.8)$$

Finally, we finish our formulation complementing the scheme with appropriate boundary conditions selected from above and initial condition

$$\mathbf{u}(\mathbf{x}, 0) = \mathbf{u}_0(\mathbf{x}).$$

¹In physics the dissipation stays for the loss of wave energy, with consequent decrease in wave amplitude, due to wave breaking, turbulence, and viscous effects.

5.2 Numerical test

Within this section we inspect the stability and convergence of a normalized TE-mode of Maxwell's equations²

$$\begin{aligned}\frac{\partial E_x}{\partial t} &= \frac{\partial H_z}{\partial y}, \\ \frac{\partial E_y}{\partial t} &= -\frac{\partial H_z}{\partial x}, \\ \frac{\partial H_z}{\partial t} &= \frac{\partial E_x}{\partial y} - \frac{\partial E_y}{\partial x}.\end{aligned}\tag{5.9}$$

All experiments shall be performed on domain $\Omega = [-1, 1]^2$ whose partition is described in Table 5.1. The meshes in Table 5.1 are constructed using MATLAB[®] function `delaunay` that creates the so-called Delaunay's triangulation (see [24]). In Fig. 5.1 are shown some of them³.

Using the same terminology as in Chapter 4 one can easily derive a local strong semi-discrete form of Eqs.(5.9)

$$\begin{aligned}\frac{d}{dt}E_h^x &= \mathcal{M}S_y H_h^z \\ &\quad - \frac{1}{2}(J\mathcal{M})^{-1} \oint_{\partial T_k} (n_y[H_h^z] + \alpha(n_x[E_h^x] + n_y[E_h^y] - [E_h^x]))\ell_i^k d\mathbf{x}, \\ \frac{d}{dt}E_h^y &= -\mathcal{M}S_x H_h^z \\ &\quad + \frac{1}{2}(J\mathcal{M})^{-1} \oint_{\partial T_k} (n_x[H_h^z] + \alpha(n_x[E_h^x] + n_y[E_h^y] - [E_h^y]))\ell_i^k d\mathbf{x}, \\ \frac{d}{dt}H_h^z &= \mathcal{M}S_y E_h^x - \mathcal{M}S_x E_h^y \\ &\quad + \frac{1}{2}(J\mathcal{M})^{-1} \oint_{\partial T_k} (n_x[E_h^y] - n_y[E_h^x] - \alpha[H_h^z])\ell_i^k d\mathbf{x}\end{aligned}\tag{5.10}$$

Moreover, the Eqs.(5.10) have a compact form

$$\frac{d}{dt}\mathbf{u}_h = \mathcal{L}_h(\alpha)\mathbf{u}_h.\tag{5.11}$$

For a fixed mesh, it is clear that operator \mathcal{L}_h depends only on the parameter α .

TABLE 5.1: Description of meshes used for computations of error.

Minimal distance between two vertices h_{min}	0.70	0.56	0.28	0.14	0.07
Number of triangles K	32	50	200	800	3200
Number of vertices N_v	25	36	121	441	1681

²This form can be obtained by making dimensionless each quantity that appears in initial equations. Informally speaking, we consider $\varepsilon = \text{diag}(1, 1)$ and $\mu = 1$.

³Let us note that a *shortest distance* between two nodes in a 2D mesh, obtained by a triangulation, represents the minimal of all maximal triangle edges. For instance, the shortest distance of a mesh in Fig. 5.1 is the hypotenuse of triangle.

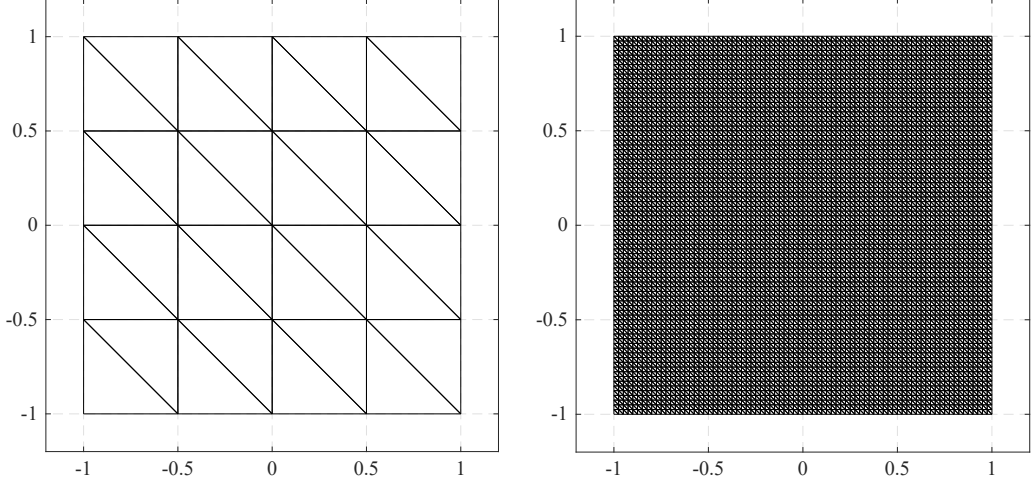


FIGURE 5.1: Example of meshes used in numerical experiments for $K = 32$ and $K = 3200$.

5.2.1 Stability

We are going to illustrate the behavior of spectrum of the DG operator \mathcal{L}_h mentioned in Eq.(5.11) and compare the results with the stability regions of the ERK methods stated before.

The mesh used for computations is given in Fig. 5.1(left) and has 32 elements, while the polynomial order is chosen to be $N = 4$. In this case, the number of interpolation points on each triangle T_k is $N_p = (N + 1)(N + 2)/2 = 15$. Since there are three fields whose solution is unknown, the DG discrete operator size is $K \times N_p \times 3 = 1440$. Hence, each of Fig. 5.2–5.3 has 1440 eigenvalues denoted by blue asterisk.

In Fig. 5.2–5.3 are used PMC boundary conditions defined in Eq.(5.5). The estimate from Eq.(4.29) in combination with minimal inscribed circle diameter of triangles in mesh denoted by r_T [15],

$$\Delta t = \min_{\Omega_h} r_T(\mathbf{x}) \frac{2}{3} \min_i \Delta r_i, \quad (5.12)$$

is used for temporal step size.

As we may see in Fig. 5.2–5.3, the time-step defined in Eq.(5.12) keeps the scheme stable. Furthermore, LSERK(14, 4) allows even bigger steps in time.

Note that, by decreasing the parameter α , the spectrum is getting stick to the imaginary axis. Consequently, for $\alpha = 0$ all eigenvalues become pure imaginary. This is a result of the energy-conserving nature of central flux [10].

5.2.2 Convergence

Let us begin by proposing an exact solution of the system of Eqs.(5.9) [18]

$$\begin{aligned} E_x^*(x, y, t) &= -\frac{1}{\sqrt{2}} \cos(\pi x) \sin(\pi y) \sin(\pi\sqrt{2}t), \\ E_y^*(x, y, t) &= \frac{1}{\sqrt{2}} \sin(\pi x) \cos(\pi y) \sin(\pi\sqrt{2}t) \\ H_z^*(x, y, t) &= \cos(\pi x) \cos(\pi y) \cos(\pi\sqrt{2}t). \end{aligned} \quad (5.13)$$

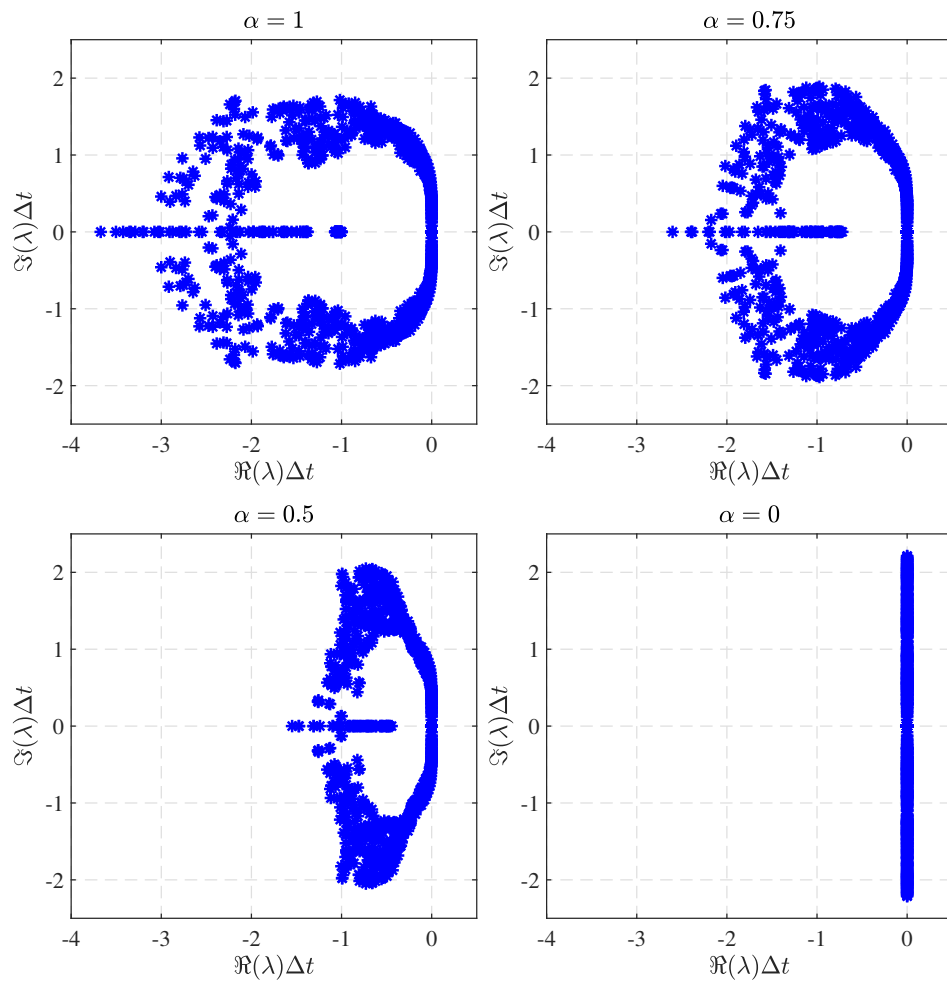


FIGURE 5.2: Spectrum of DG operator for TE-mode of Maxwell's equations.

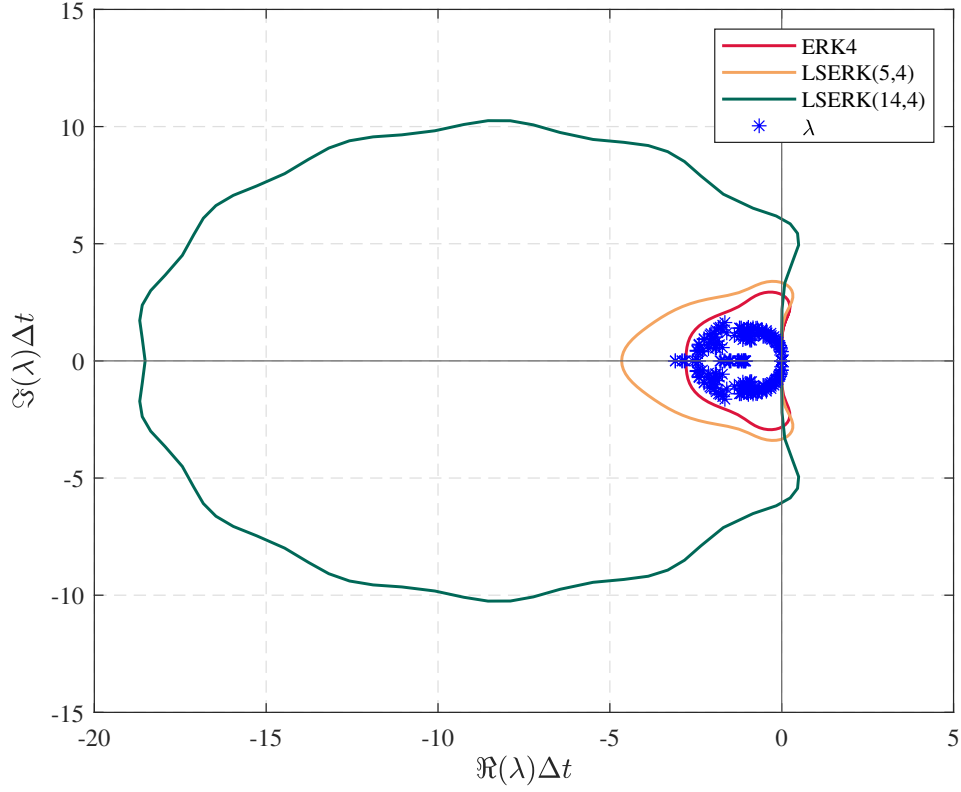


FIGURE 5.3: Spectrum of DG operator in stability regions of ERK methods.

For purposes of convergence analysis we assume PEC boundary conditions given by Eq.(5.4), while initial conditions are set as

$$\begin{aligned} E_x(x, y, 0) &= 0, \\ E_y(x, y, 0) &= 0, \\ H_z(x, y, 0) &= \cos(\pi x) \cos(\pi y). \end{aligned}$$

In our tests, we distinguish upwind and central scheme. The final time is chosen to be $T = 0.1$ for all trials in space. For each field in TE-mode and corresponding exact solution given in Eq.(5.13), we define L^2 -error of approximation separately for the fields

$$\begin{aligned} \text{Error}(E_x) &= \|E_x^* - E_h^x\|_{L^2(\Omega)}, \\ \text{Error}(E_y) &= \|E_y^* - E_h^y\|_{L^2(\Omega)}, \\ \text{Error}(H_z) &= \|H_z^* - H_h^z\|_{L^2(\Omega)}, \end{aligned}$$

while the error of solution vector $\mathbf{u}_h = (E_h^x, E_h^y, H_h^z)$ is

$$\text{Error}(u_h) = \sqrt{\text{Error}(E_x) + \text{Error}(E_y) + \text{Error}(H_z)}.$$

The order of convergence in space is determined from

$$\frac{\log(\text{Error}(u_{h,\Delta t})/\text{Error}(u_{h',\Delta t}))}{\log(h/h')},$$

where $u_{h,\Delta t}$ represents approximate solution calculated for time-step Δt , while h and h' are diameters of two consecutive meshes. From the other side, if Δt and $\Delta t'$ are two

TABLE 5.2: L^2 -error and spatial order of convergence.

α	N	K	h	Error(u_h)	Order
0	1	32	7.07E-01	4.38E-01	–
		50	5.66E-01	3.82E-01	0.61
		200	2.83E-01	1.78E-01	1.10
		800	1.41E-01	7.32E-02	1.28
		3200	7.07E-02	3.81E-02	0.94
	2	32	7.07E-01	1.82E-01	–
		50	5.66E-01	1.17E-01	1.99
		200	2.83E-01	2.25E-02	2.38
		800	1.41E-01	4.77E-03	2.24
		3200	7.07E-02	1.14E-03	2.07
	3	32	7.07E-01	4.31E-02	–
		50	5.66E-01	2.01E-02	3.42
		200	2.83E-01	2.42E-03	3.05
		800	1.41E-01	2.97E-04	3.03
		3200	7.07E-02	3.73E-05	3.00
	4	32	7.07E-01	7.99E-03	–
		50	5.66E-01	3.03E-03	4.35
		200	2.83E-01	1.81E-04	4.06
		800	1.41E-01	1.10E-05	4.04
		3200	7.07E-02	6.80E-07	4.01
1	1	32	7.07E-01	3.25E-01	–
		50	5.66E-01	2.45E-01	1.26
		200	2.83E-01	6.75E-02	1.86
		800	1.41E-01	1.57E-02	2.10
		3200	7.07E-02	3.90E-03	2.01
	2	32	7.07E-01	1.01E-01	–
		50	5.66E-01	6.58E-02	1.90
		200	2.83E-01	1.11E-02	2.57
		800	1.41E-01	1.09E-03	3.35
		3200	7.07E-02	1.44E-04	2.92
	3	32	7.07E-01	2.43E-02	–
		50	5.66E-01	1.09E-02	3.59
		200	2.83E-01	8.68E-04	3.65
		800	1.41E-01	3.74E-05	4.54
		3200	7.07E-02	2.40E-06	3.96
	4	32	7.07E-01	3.87E-03	–
		50	5.66E-01	1.44E-03	4.43
		200	2.83E-01	4.50E-05	5.00
		800	1.41E-01	1.44E-06	4.97
		3200	7.07E-02	5.11E-08	4.82

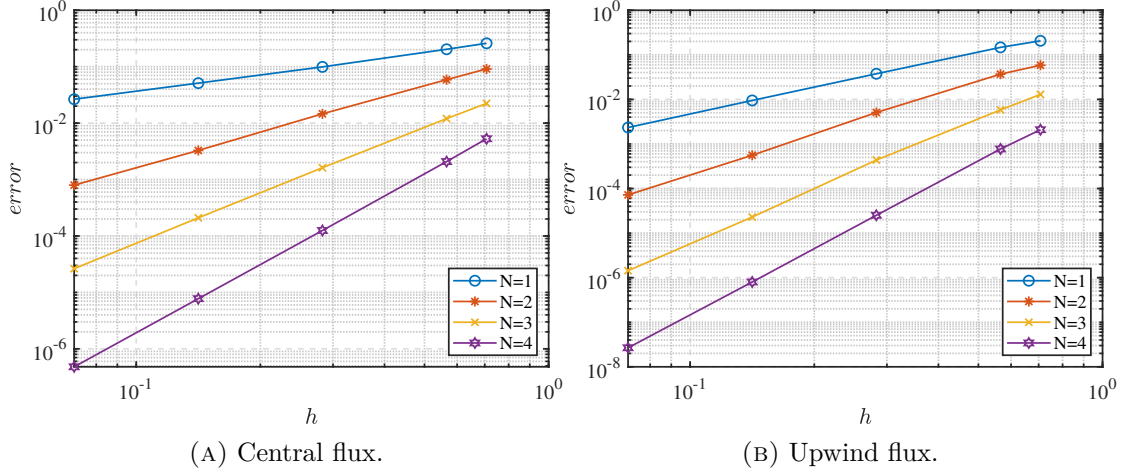


FIGURE 5.4: L^2 -error for field E_x versus h .

different time-step sizes for a fixed diameter of mesh h , then the order of convergence in time is

$$\frac{\log(\text{Error}(u_{h,\Delta t})/\text{Error}(u_{h,\Delta t'}))}{\log(\Delta t/\Delta t')}.$$

In Table 5.2 the L^2 -errors between approximate and exact solution of Eqs.(5.9) are computed as well as associated orders of convergence in space. The computations are performed on different meshes, all given in Table 5.1, for both central ($\alpha = 0$) and upwind ($\alpha = 1$) flux, while polynomial orders varied from first to fourth. The time-step is set to be $\Delta t = 10^{-4}$. In Fig. 5.4 data from Table 5.2 is visualized only for the component of electric field E_x , into a plot whose axes are logarithmically scaled. As we may see, while central flux is used, the order of approximation is around $\mathcal{O}(h^N)$, whereas space discretizations that use upwind flux in most of cases achieve the order $\mathcal{O}(h^{N+1})$, all in accordance to theoretical results presented in literature (see [1] and the references therein).

TABLE 5.3: L^2 -error and temporal order of convergence.

Δt	Error(u_h)	Order
9.00E-03	3.41E-10	—
4.50E-03	2.14E-11	4.00
2.25E-03	1.33E-12	4.00
1.12E-03	8.33E-14	4.00

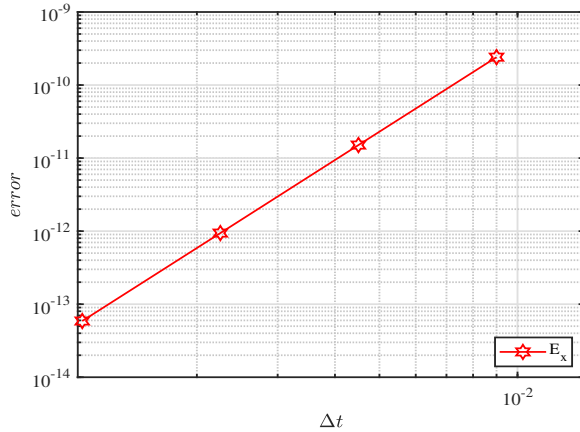


FIGURE 5.5: L^2 -error for field E_x versus Δt .

Further, Table 5.3 shows that the temporal discretization gives the fourth order approximation, *i.e.* as expected the order is $\mathcal{O}(\Delta t^4)$. Namely, we have fixed the polynomial order to $N = 8$, whereas the number of elements in mesh is $K = 3200$ (see Fig. 5.1(right)). In Fig. 5.5, the results obtained in Table 5.3 are illustrated, but again only for x -direction of electric field. Clearly, the central and upwind schemes give the same

results. Lastly, we have to emphasize that both low-storage explicit Runge–Kutta methods, LSERK(5, 4) and LSERK(14, 4), give the same values of entries in Tables 5.2–5.3 as it may be naturally expected.

5.3 Modelling scattered electromagnetic wave's propagation in 2D

In this subsection we will propose a computational model that mimics the electromagnetic wave's propagation through eye's tissues in order to create a virtual OCT scan. As OCT standard techniques only provide structural information, it is necessary to expand OCT data analysis to account for both structural and functional information [29]. A mathematical modelling of OCT data could expand the information provides by OCT from structural to functional information. The functional information may provide a means for optical biopsy [13], as well as contributing to an earlier diagnosis and, hopefully, a more efficient treatment [29].

The corneal stroma is composed of dense, regularly packed collagen fibrils arranged in layers or lamellae. Fibrils are narrow, uniform in diameter and precisely organized. These properties are vital to maintain transparency and to provide the biomechanical prerequisites necessary to sustain shape and provide strength [23]. There is a vast literature trying to figure out why cornea is transparent [21, 4, 14, 23], but there is a consensus that every model trying to explain corneal transparency should consider the shape, size and organization of EMC in the corneal stroma and its elements such as collagen fibrils and proteoglycans, and their refractive indices.

In this section we simulate the light scattering in the human's cornea aiming to mimicking the OCT imaging system. We consider a two-dimensional model of backscattered light intensity in two different scenarios that correspond to the fibrils organization presented in Fig. 5.6. Namely, our simulation settings are composed of 38 randomly disturbed collagen fibrils, which are denoted by circles in mentioned figure. Fig. 5.6(left) refers to a healthy human cornea that has fibrils of diameter $31nm$, while the distance between every two adjacent fibrils is not less than its doubled diameter. In Fig. 5.6(right), that tries to mimic a pathologic situation, positions of fibrils are kept, while 20% of overall number of fibrils (≈ 8 fibrils) are chosen to have doubled diameter [23].

The natural approach for modelling of the electromagnetic radiation is to consider Maxwell's equations. Since we want simulate the OCT imaging system, we use so-called scattered field formulation, Eqs.(3.8), previously considered in Chapter 3,

$$\begin{aligned}\varepsilon_{xx}\frac{\partial E_x^{sc}}{\partial t} + \varepsilon_{xy}\frac{\partial E_y^{sc}}{\partial t} &= \frac{\partial H_z^{sc}}{\partial y} + P(x, y, t), \\ \varepsilon_{yx}\frac{\partial E_x^{sc}}{\partial t} + \varepsilon_{yy}\frac{\partial E_y^{sc}}{\partial t} &= -\frac{\partial H_z^{sc}}{\partial x} + Q(x, y, t), \\ \mu\frac{\partial H_z^{sc}}{\partial t} &= -\frac{\partial E_y^{sc}}{\partial x} + \frac{\partial E_x^{sc}}{\partial y} + R(x, y, t),\end{aligned}\tag{5.14}$$

with sources

$$\begin{aligned}P(x, y, t) &= (\varepsilon^{inc} - \varepsilon_{xx})\frac{\partial E_x^{inc}}{\partial t} - \varepsilon_{xy}\frac{\partial E_y^{inc}}{\partial t}, \\ Q(x, y, t) &= -\varepsilon_{yx}\frac{\partial E_x^{inc}}{\partial t} + (\varepsilon^{inc} - \varepsilon_{yy})\frac{\partial E_y^{inc}}{\partial t}, \\ R(x, y, t) &= (\mu^{inc} - \mu)\frac{\partial H_z^{inc}}{\partial t}.\end{aligned}\tag{5.15}$$

Here, the scattered fields E_x^{sc} , E_y^{sc} and H_z^{sc} is being solved, while the incident fields are the following

$$\begin{aligned} E_x^{inc}(x, y, t) &= 0, \\ E_y^{inc}(x, y, t) &= \cos(10(x - t)), \\ H_z^{inc}(x, y, t) &= 0. \end{aligned}$$

Further, on the computational (dimensionless) domain $\Omega = [-1, 1]^2$ we define a union of circles \mathcal{F} that model healthy corneal collagen fibrils' positions, while Ω/\mathcal{F} states for EMC stromal components or simply, the background cells. Similarly, for ill case we define the set \mathcal{F}' . These sets are collectively illustrated in Fig. 5.6. The radius of each fibril is 0.03 with exception in cases where diameter of fibril is doubled and takes value 0.06. The assumption about distance constrain is also fulfilled.

Due to corneal optical anisotropy exposed in Chapter 2, we consider a diagonal piecewise constant permittivity tensor, *i.e.*, entries ε_{xy} and ε_{yx} are zero. Since the corneal tissues properties were already studied for a couple of centuries, range of some quantities is well-standardized, such as refractive indices of collagen fibrils and EMC cells. The exact values of refractive indices for these two types of tissue are specified by discussion with scientists that deal with medical aspect of the bigger research project which is used as an inspiration for this thesis. Finally, using the connection between refractive indices and dielectric permittivity constant established in Subsection 2.4.1, we define diagonal entries of anisotropic dielectric tensor

$$\varepsilon_{xx}(x, y) = \varepsilon_{yy}(x, y) = \begin{cases} (1.55)^2, & (x, y) \in \mathcal{F} \quad \text{and} \quad (x, y) \in \mathcal{F}', \\ (1.345)^2, & (x, y) \in \Omega/\mathcal{F} \quad \text{and} \quad (x, y) \in \Omega/\mathcal{F}'. \end{cases}$$

This yields $\varepsilon^{inc} = (1.345)^2$. Since eye's tissues are non-magnetic medium, the dielectric permeability is $\mu = \mu^{inc} = 1$.

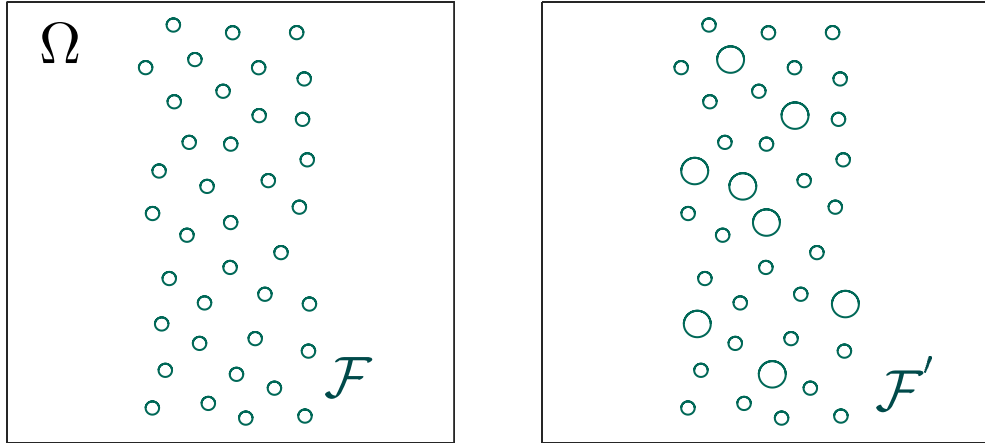


FIGURE 5.6: Stromal collagen fibrils arrangement. See text for further discussion.

In what concerns the boundary, we consider the SM-ABC, Eq.(5.8), that minimizes reflections on the border of the computational domain. The initial conditions are chosen to be zero.

The spatial discretization of Eqs.(5.14)–(5.15) is done on meshes⁴ defined in Fig. 5.7 using DG method coupled with upwind flux ($\alpha = 1$). The LSERK(14, 4) is applied for

⁴This meshes are made using software FreeFem++[®].

time integration with step $\Delta t = 10^{-3}$. The solution is approximated by polynomial of order $N = 4$. The final simulation time is $T = 1$.

An evolution in time of scattered electric field intensity

$$I^{sc} = \sqrt{(E_x^{sc})^2 + (E_y^{sc})^2}$$

is displayed in Fig. 5.8. As it may be seen in the figures, the backscattering is more intensive in case where the organization of the fibrils is not uniform (Fig. 5.6(right)). This corresponds to a lack of transparency of the ill cornea.

Additionally, for purpose of a deeper analysis, in Fig. 5.9 is done the horizontal cut at $y = 0$ of approximate solution obtained in Fig. 5.8. As we may see, 20% of total number of stromal fibrils is enough to augment the background scattering of radiation that later causes swelling of cornea and lose of its transparency, as theoretically stated in [23]. Furthermore, the backscattering is even more excited in Fig. 5.10 where the cut is done at $y = 0.1$.

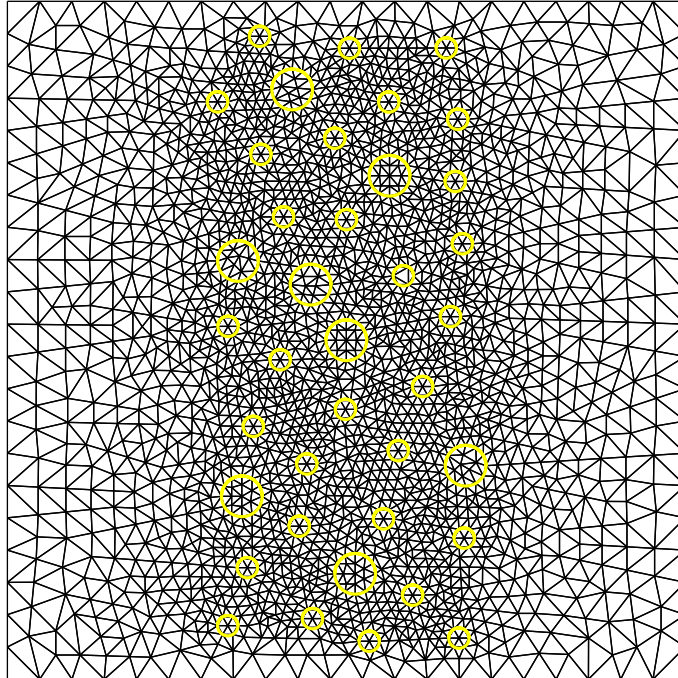
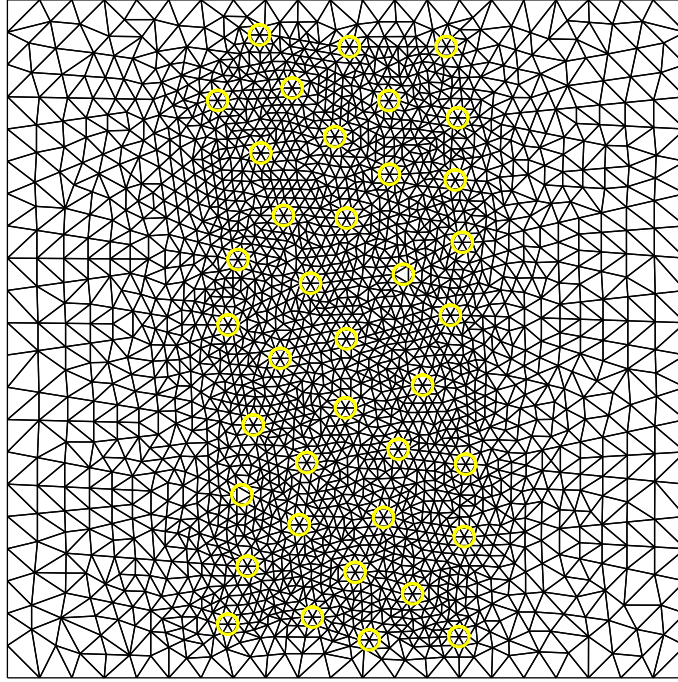


FIGURE 5.7: Meshes used in simulations for setup given in Fig. 5.6. The mesh above contains $K = 5072$ triangles and corresponds to the left arrangement in Fig. 5.6, while the mesh below matches with the right fibrils arrangement and counts $K = 4972$ elements.

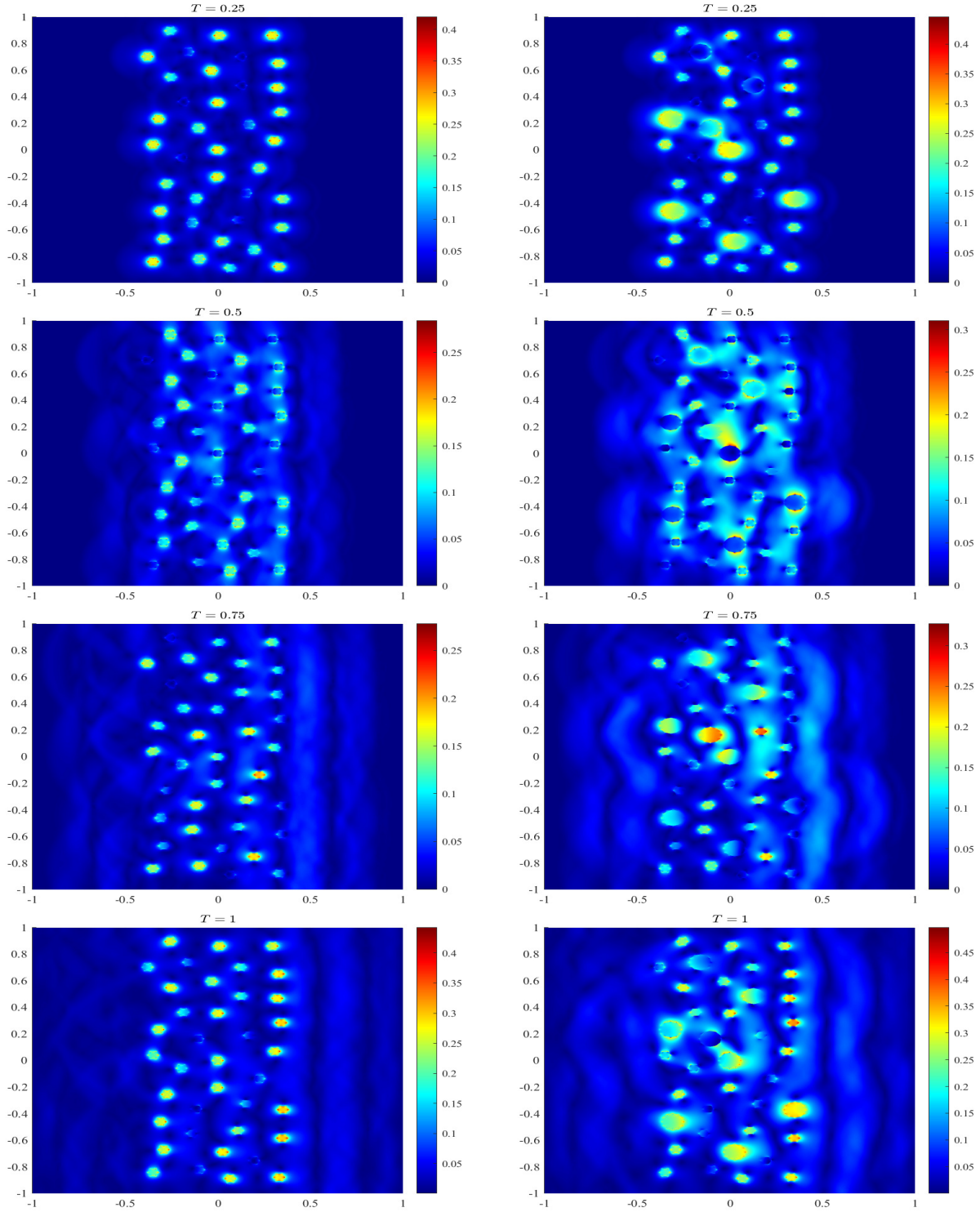


FIGURE 5.8: Time evolution of scattered electric field intensity I^{sc} . Left hand side corresponds to healthy cornea, whereas right hand side states for case of corneal illness.

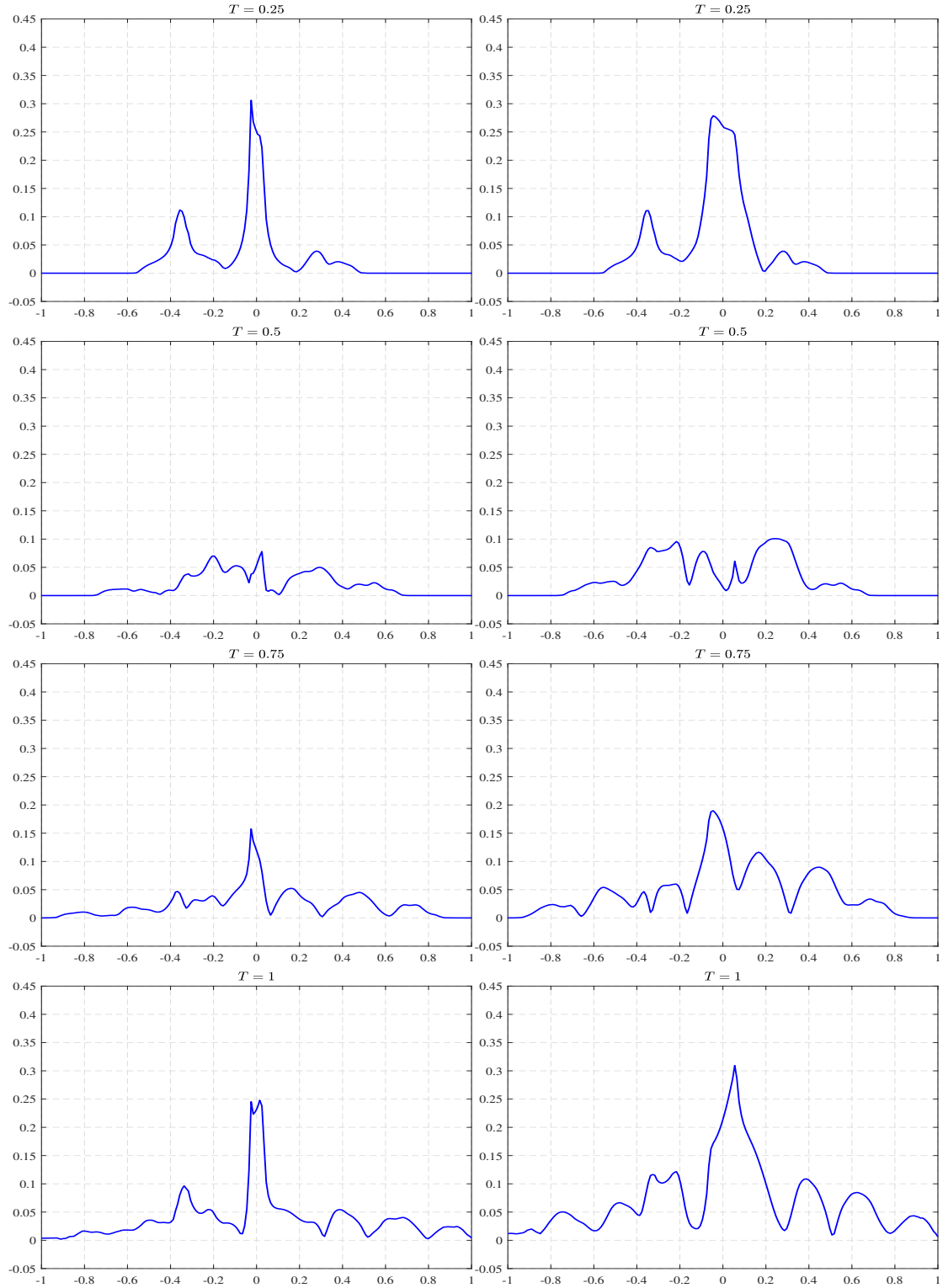


FIGURE 5.9: Horizontal cut of field I^{sc} from Fig. 5.8 at $y = 0$.

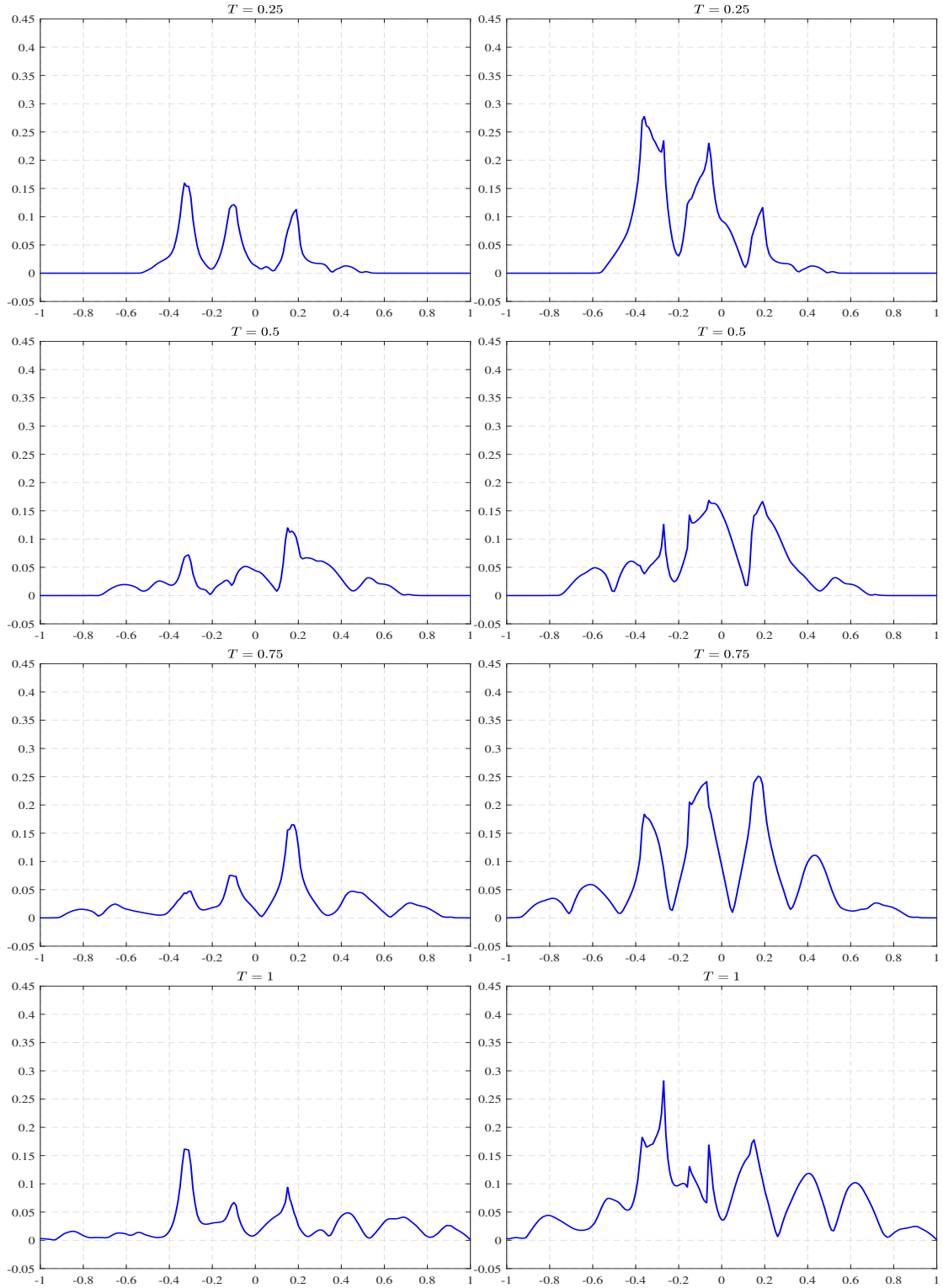


FIGURE 5.10: Horizontal cut of field I^{sc} from Fig. 5.8 at $y = 0.1$.

Chapter 6

Conclusion

Through this work we dealt with a problem arising in ophthalmology and gave the appropriate theoretically based model. Since the model had required a knowledge originating from multidisciplinary sciences, we introduced ourselves with many new concepts.

First of all, it was necessary to learn basic anatomy of eye with main accent on its anterior part. The corneal content was studied in more detail, and the latest understandings related to corneal transparency were exposed. The mechanism of a diagnostic device, the OCT machine, was also depicted. OCT technology had requested a comprehension of electromagnetic radiation, thus we gave the overview of electromagnetism and studied its governing equations. Classification of mediums in which electromagnetic waves propagate was given, and their optical properties were explored. Having overcome these terms, we traversed to mathematical model formulation, and afterwards, to the presentation of numerical procedure.

The solving of model equations was split in space and time evaluation. Although numerical technique used in space, DG method, was quite demanding, we used an approach that could give to a reader, new to this field, the most efficient and complete explanation. For this reason, we had decided to demonstrate the numerical method on conservation law type of equations. The theoretical backup in view of mathematical proof was also provided. To complete overall numerical method, we introduced the Runge–Kutta time integrators. A comparison of stability regions of some RK methods were also proposed. The stability and convergence of these two coupled methods, *i.e.* RKDG method, was justified on Maxwell’s equations. We saw that such a discretization gives high–order accuracy.

Finally, a simulation of light scatter in corneal stroma of human eye was presented. Electromagnetic radiation during an OCT scan was compared for setups of healthy and ill human cornea. The matching with assumptions of theoretical model was found.

In order to improve the mesh quality and at the same time to constrain computational costs, the author explored several available 2D mesh generator software packages. A possible hint to cope the lack of mesh quality is to consider a different strategy in a future attempts.

The proposed simulation could be in future upgraded with increased number of fibrils such that entire lamella is presented. Moreover, it would be interesting to make a simulation in three dimensions that may illuminate a 3D–OCT image. In such case, the circles from 2D computational domain should be replaced with tiny cylinders. All these ideas lead to large scale simulations and use of parallel computers. Another direction in future research would be replacement of RKDG method with simultaneous DG discretization in both, space and time, *i.e.* so–called space–time DG method, due to its geometry flexibility and high–order accuracy.

References

- [1] Araújo, A., Barbeiro, S., & Galati, M. Kh., “Stability of a leap–frog discontinuous Galerkin method for time–domain Maxwell’s equations in anisotropic materials”, *Communications in Computational Physics* **21**(5), pp. 1350–1375, 2017
- [2] Ascher, U.M. & Petzold, L.R., “Computer Methods for Ordinary Differential Equations and Differential–Algebraic Equations”, SIAM, 1998
- [3] Batista, A., “Two–photon imaging of the cornea using femtosecond laser microscopes and tomographs”, PhD Dissertation, Faculty of Natural Sciences and Technology of the Saarland University, Germany, 2018
- [4] Benedek, G.B., “Theory of transparency of the eye”, *Applied Optics* **10**, pp. 459–473, 1971
- [5] Bernardi, C. & Maday, Y., “Polynomial interpolation results in Sobolev spaces”, *J. Comput. Appl. Math.* **43**, pp. 53–80, 1992
- [6] Canuto, C., Hussaini, M.Y., Quarteroni, A., Zang, Th.A., “Spectral Methods: Fundamentals in Single Domains”, Springer–Verlag, Berlin Heidelberg, 2006
- [7] Carpenter, M.H. & Kennedy, C.A., “Fourth–order 2N–storage Runge–Kutta schemes”, NASA Report TM 109112, NASA Langley Research Center, 1994
- [8] Cockburn, B., Karniadakis, G. & Shu, C.–W., “The development of discontinuous Galerkin methods” in: “Discontinuous Galerkin Methods: Theory, Computation and Applications”, *Lecture Notes in Computational Science and Engineering* **11**, Springer, Part I: Overview, pp. 3–50, 2000
- [9] Courant, R., Friedrichs, K. & Lewy, H., “Über die partiellen Differenzengleichungen der mathematischen Physik”, *Mathematische Annalen* (in German) **100**(1), pp. 32–74, 1928
- [10] Diehl, R., Busch, K., & Niegemann, J., “Comparison of Low–Storage Runge–Kutta Schemes for Discontinuous Galerkin Time–Domain Simulations of Maxwell’s Equations”, *Journal of Computational and Theoretical Nanoscience* **7**(8), pp. 1572–1580, 2010
- [11] Drexler, W. & Fujimoto, J. G., “Introduction to OCT” in: “Optical Coherence Tomography: Technology and Applications, Second Edition”, pp. 3–64, Springer International Publishing, 2015
- [12] Evans, L.C., “Partial Differential Equations”, American Mathematical Society, Providence, RI, 1998
- [13] Ghalati, M. Kh., “Numerical Analysis and Simulation of Discontinuous Galerkin Method for the Time–Domain Maxwell’s Equations”, PhD thesis, Universidade de Coimbra, Portugal, 2017

- [14] Hart, R.W. & Farrell, R.A., “Light scattering in the cornea”, *Journal of the Optical Society of America* **59**(6), pp. 766–774, 1969
- [15] Hesthaven, J.S. & Warburton, T., “Nodal Discontinuous Galerkin Methods: Algorithms, Analysis, and Applications”, *Springer Texts in Applied Mathematics* 54, Springer Verlag, New York, 2008
- [16] Huang, D., Li, Y. & Tang, M., “Anterior eye imaging with optical coherence tomography” in: “Optical Coherence Tomography: Technology and Applications, Second Edition”, pp. 1649–1683, Springer International Publishing, 2015
- [17] Jin, J.M., “Theory and Computation of Electromagnetic Fields”, 1st ed., Wiley–IEEE Press, 2010
- [18] König, M., Busch, K. & Niegemann, J., “The Discontinuous Galerkin Time–Domain method for Maxwell’s equations with anisotropic materials”, *Photonics and Nanostructures – Fundamentals and Applications* **8**, pp. 303–309, 2010
- [19] Kreiss, H.O. & Wu L., “On the stability definition of difference approximations for the initial boundary value problem”, *Applied Numerical Mathematics* **12**, pp. 213–227, 1993
- [20] Lax, P. D. & Richtmyer, R. D., “Survey of the Stability of Linear Finite Difference Equations”, *Comm. Pure Appl. Math.* **9**, pp. 267–293, 1956
- [21] Maurice, D.,M., “The structure and transparency of the cornea”, *The Journal of physiology* **136**(2), pp. 263–286, 1957
- [22] Meek, K.M., “The cornea” in: “Signal and perception: The fundamentals of human sensation”, Roberts, D., Palgrave MacMillan, The Open University, pp. 103–114, 2002
- [23] Meek, K.M. & Knupp, C., “Corneal structure and transparency”, *Progress in Retinal and Eye Research* **49**, pp. 1–16, 2015
- [24] Mavriplis, D. J., “Mesh generation and adaptivity for complex geometries and flows” in: “Handbook of computational fluid mechanics”, Academic Press, pp. 417–459, 1996
- [25] Maxwell, J. C., “A treatise on electricity and magnetism”, UK:Oxford University Press, 1873
- [26] Niegemann, J., König, M., Stannigel, K., & Busch, K., “Higher–order time–domain methods for the analysis of nano–photonic systems”, *Photonics and Nanostructures–Fundamentals and Applications* **7**(1), pp. 2–11, 2009
- [27] Niegemann, J., Diehl, R., & Busch K., “Efficient low–storage Runge–Kutta schemes with optimized stability regions”, *Journal of Computational Physics* **231**, pp. 364–372, 2012
- [28] Reed, W. H. & Hill, T. R., “Triangular Mesh methods for the Neutron Transport Equation”, Los Alamos Scientific Laboratory Report LA–UR–73–479, 1973
- [29] Santos, M., Araújo, A., Barbeiro, S., Caramelo, F., Correia, A.L., Marques, I., Pinto, L., Serranho, P., Bernardes, R. & Morgado, M., “Simulation of Cellular Changes on Optical Coherence Tomography of Human Retina”, 37th Annual International Conference of the IEEE Engineering in Medicine and Biology Society (EMBC), Milan, pp. 8147–8150, August 2015

- [30] Serranho, P., Morgado, M., & Bernardes, R., “Optical coherence tomography: a concept review” in: “Optical coherence tomography: A clinical and technical update”, Springer–Verlag, pp. 139–156, 2012
- [31] Taflove, A. & Hagness, S.C., “Computational Electrodynamics: The Finite–Difference Time–Domain method”, 3rd ed., Artech House, 2005
- [32] Yang, D.K. & Wu, S.T., “Fundamentals of Liquid Crystal Devices, Second Edition”, Wiley, 2014

Curriculum Vitae

Sunčica Sakić was born on September 29, 1995 in Novi Kneževac, Serbia. However, she grown up in Temerin, Serbia, where she finished her primary and secondary education. She received her Bachelors degree in Mathematics in 2018 at Faculty of Sciences, University of Novi Sad (UNS), Serbia. In the same year, she decides to continue her studies at the same faculty, but this time in field of Applied Mathematics.

In the first year of Master studies, she got opportunity to work on the project ‘How to exploit losses – heating by magnetic induction’ as a participant of 33rd ECMI (European Consortium for Mathematics in Industry) Modelling Week held at TU Darmstadt in Germany. In January 2020, she passed all the exams at UNS including those which provide a specialized degree in Technomathematics that issues as a diploma supplement. She spent the period February–July 2020 doing research for her thesis at University of Coimbra (UC) in Portugal under the Erasmus+ grant. In June 2020 at UC she passed her last exam of Master program and formed the GPA 9.87/10.00. Defence of this thesis will assure to her a certificate awarded by ECMI. In October 2020 she will became a PhD student in Computational Mathematics at Charles University in Prague, Czech Republic.



Novi Sad, 2020

Sunčica Sakić

UNIVERZITET U NOVOM SADU
PRIRODNO–MATEMATIČKI FAKULTET
KLJUČNA DOKUMENTACIJSKA INFORMACIJA

Redni broj:

RBR

Identifikacion broj:

IBR

Tip dokumentacije:

monografska dokumentacija

BF

Tip zapisa:

tekstualni štampani materijal

TZ

Vrsta rada:

Master rad

VR

Autor:

Sunčica Sakić

AU

Mentor:

dr Srboljub Simić

MN

Naslov rada:

Modeliranje propagacije svetlosti u očnim tkivima

NR

Jezik publikacije:

engleski

JP

Jezik izvoda:

srpski/engleski

JI

Zemlja publikovanja:

Republika Srbija

ZP

Uže geografsko područje:

Vojvodina

UGP

Godina:

2020.

GO

Izdavač:

autorski reprint

IZ

Mesto i adresa:

Novi Sad, Trg Dositeja Obradovića 4

MA

Fizički opis rada:

6 poglavlja, 65 stranica, 32 lit. citata, 25 slika

FO

Naučna oblast:

Matematika

NO

Naučna disciplina:

Matematičko modeliranje

ND

*Predmetna odrednica/
ključne reči:*

Optička koherentna tomografija, Maksvelove jednačine,
Prekidni Galerkinov metod, Matematičko modeliranje

PO

UDK:

Čuva se:

u biblioteci Departmana za matematiku i informatiku
Prirodno–matematičkog fakulteta
Univerziteta u Novom Sadu

ČU

Važna napomena:

VN

Izvod:

IZ

U proteklih nekoliko decenija, tehnike medicinskog snimanja značajno su doprinele otkrivanju unutrašnjih telesnih struktura, kao i dijagnozi i lečenju bolesti. Konkretno, u oftalmologiji, jedan popularan neinvazivan vid snimanja očnih tkiva je optička koherentna tomografija (*engl.* Optical Coherence Tomography – OCT). U ovoj tezi bavimo se modeliranjem tkiva rožnjače, čija neprozirnost i dan danas predstavlja predmet naučnog interesovanja. Naš cilj je generisati virtuelni OCT snimak, uz pomoć odgovarajućeg matematičkog modela, koji bi dalje mogao locirati uslove koji dovode do zamućenja ljudske rožnjače. Kako očna tkiva predstavljaju, fizički gledano, anizotropne materijale, model zahteva izučavanje istih. Iako je numerička analiza, prisutna u literaturi, ograničena na izotropne materijale, uspeali smo modifikovati numerički alat anizotropnom slučaju. Mehanička svojstva oka smo upotpunili uvođenjem optičkih karakteristika anizotropnih materijala, što je neophodno za razumevanje matematičkog modela u celosti. U svrhu numeričkih simulacija i analize numeričkog algoritma, razmatraju se različite vrste graničnih uslova koji se susreću u elektromagnetizmu. Numeričke simulacije se izvode primenom tzv. Runge–Kuta prekidnog Galerkinovog metoda na Maksvelove jednačine prethodno prilagođenim modelu. Predstavljena je detaljna analiza dobijenih rezultata. Veliki deo rada čini izučavanje materije prekidnog Galerkinovog metoda (*engl.* discontinuous Galerkin – DG), procedure koja pripada metodima konačnih elemenata. DG metod se primenjuje na prostornoj diskretizaciji, dok vremenskoj promenljivoj pristupamo koristeći eksplicitni Runge–Kuta metod. Na ovaj način dobijamo potpunu diskretizaciju početnih jednačina. Konvergencija i stabilnost ovih metoda su dobro ispitani i numerički testirani na različitim šemama definisanim na različitim mrežama diskretizacije.

*Datum prihvatanja teme
od strane NN veća:*

13.07.2020.

DP

Datum odbrane:

01.09.2020.

DO

Članovi komisije:

KO

Predsednik: dr Ivana Vojnović, docent,
Prirodno–matematički fakultet,
Univerzitet u Novom Sadu
Član: dr Marko Nedeljkov, redovni profesor,
Prirodno–matematički fakultet,
Univerzitet u Novom Sadu
Član: dr Srboljub Simić, redovni profesor,
Prirodno–matematički fakultet,
Univerzitet u Novom Sadu
Član: dr Adérito Araújo, vanredni profesor,
Naučno–tehnološki fakultet,
Univerzitet u Koimbri, Portugal

UNIVERSITY OF NOVI SAD
FACULTY OF SCIENCES
KEY WORD DOCUMENTATION

Accession number:

ANO

Identification number:

INO

Document type:

monograph type

DT

Type of record:

printed text

TR

Contents code:

Master thesis

CC

Author:

Sunčica Sakić

AU

Mentor:

Srboljub Simić, PhD

MN

Title:

Modelling Light Propagation In Ocular Tissues

TI

Language of text:

English

LT

Language of abstract:

serbian/english

LA

Country of publication:

Republic of Serbia

CP

Locality of publication:

Vojvodina

LP

Publication year:

2020

PY

Publisher:

author's reprint

PU

Publication place:

Novi Sad, Trg Dositeja Obradovića 4

PP

Physical description:

6 chapters, 65 pages, 32 references, 25 figures

PD

Scientific field:

Mathematics

SF

Scientific discipline:

Mathematical Modelling

SD

Subject/Key words:

Optical Coherence Tomography, Maxwell's equations,
Discontinuous Galerkin Method, Mathematical Modelling

SKW

UC:

Holding data:

Department of Mathematics and Informatics' Library,
Faculty of Sciences, University of Novi Sad

HD

Note:

N

Abstract:
AB

In the past few decades, the medical imaging techniques have made significant contribution to the revealing of internal body structures as well as the diagnosis and treatment of disease. Specifically, in ophthalmology, one of the popular non-invasive means of ocular tissue imaging is the Optical Coherence Tomography (OCT). In this thesis we deal with the modelling of the corneal tissues whose opacity is subject of interest among scientists still today. Our goal is to generate a virtual OCT scan using an appropriate mathematical model which could further locate conditions that lead to clouding of the human cornea. Since eye's structures, in physical sense, represent anisotropic materials, the model requires the study of such materials. Although the numerical analysis, present in the literature, is restricted to isotropic materials, we will modify the computational tool to the anisotropic case. Comprehension of optical eye's properties is certainly necessary to establish a mathematical model. For the purpose of numerical simulations and analysis of the numerical algorithm, different types of boundary conditions encountered in electromagnetism are considered. Numerical simulations are performed by applying so-called Runge-Kutta discontinuous Galerkin method on Maxwell's equations previously adapted to the model. A detailed analysis of obtained results is presented. A large part of thesis is occupied by the proposition of discontinuous Galerkin (DG) method, a procedure that belongs to the family of finite element methods. The DG method is applied on spatial discretization, while an explicit Runge-Kutta method is employed for temporal integration. In this way we get a full discretization of initial equations. In addition, convergence and stability of these methods are well studied and numerically tested on various schemes defined different meshes.

Accepted by
the Scientific Board on: July 13, 2020
ASB

Defended: September 1, 2020
DE

Thesis defend board:
DB

<i>President:</i>	Ivana Vojnović, PhD, Assistant Professor, Faculty of Sciences, University of Novi Sad
<i>Member:</i>	Marko Nedeljkov, PhD, Full Professor, Faculty of Sciences, University of Novi Sad
<i>Member:</i>	Srboljub Simić, PhD, Full Professor, Faculty of Sciences, University of Novi Sad
<i>Member:</i>	Adérito Araújo, PhD, Associate Professor, Faculty of Sciences and Technology, University of Coimbra, Portugal